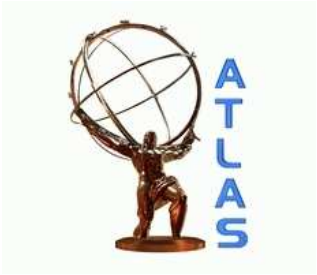

ATLAS NOTE

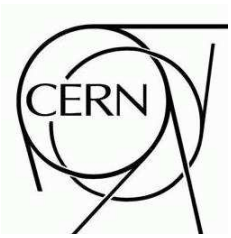

July 10, 2009

The Impact of Inner Detector and Muon Spectrometer Misalignments on Selected Physics Processes

Eva Bouhova-Thacker[1], James Catmore[1], Susan Cheatham[1], Ben Cooper[2], Claudio Gatti[3], Tobias Golling[4], Grant Gorfine[5], Lee de Mora[1], Alastair Dewhurst[1], Sebastian Fleischmann[6], Roger Jones[1], Vato Kartvelishvili[1], Michael Leyton[4], Antonio Salvucci[7], Maria Smizanska[1]

ATL-PHYS-INT-2009-067
20 July 2009

Abstract

This note documents several studies which investigate the impact on physics and performance of misalignments of the ATLAS Inner Detector (ID) and Muon Spectrometer (MS). For the Inner Detector studies two different types of misalignment are used: random module-to-module misalignments and global systematic misalignments. The impact of one or both of these types of misalignment on B-physics observables, Tau performance and $Z \rightarrow \mu\mu$ reconstruction via ID tracks are investigated. For the Muon Spectrometer random chamber-to-chamber misalignments are used. The impact of these MS misalignments, along with the global systematic misalignments of the ID, on high-p_T combined and standalone muon reconstruction in the context of a Z' analysis are investigated.

1 Introduction

The ability to successfully reconstruct the trajectory of charged particles from the measurements in the Inner Detector and, in the case of muons, Muon Spectrometer is of crucial importance for many physics analyses at ATLAS. In the reconstruction of muons it is essentially the only handle we have on their four-momenta. For electrons the tracks they leave in the Inner Detector complement the information obtained from the calorimeter energy measurements and are vital for discriminating against photons. Tracking measurements are a vital part of the signature to identify hadronic tau decays, and are also crucial in the study of soft QCD physics where the low energy of the particles involved make calorimeter calibration difficult. In addition, all physics measurements rely on accurate tracking to reconstruct the 3D primary vertex of the event, and in particular the identification of B hadrons via the reconstruction of secondary vertices is vital for Top, Higgs and B-physics measurements.

The accuracy with which the trajectory of a charged particle can be reconstructed from the measurements produced in tracking detector elements is clearly highly dependent on the degree to which one knows the exact positioning and orientation of those detector elements, commonly referred to as their "alignment". In order to not degrade track parameter resolutions by more than 20% it is estimated that the position of the ID detector modules in the be known to better than 10 μm precision in the bending plane [1]. To achieve the design momentum resolution in the MS for the reconstruction of high-p_T muons each point on the track must be measured with an accuracy better than 50 μm, which implies knowing the position of each chamber to 30 μm precision [2]. However, clearly when the first collision data is taken later in 2009 the alignment of the MS and ID will not be known to this level of precision, and our experience with the Autumn 2008 cosmic ray data indicates that it could be several months or longer before this precision is achieved. Even after this time, there could still remain global systematic deformations of the ID and/or MS, so called "weak mode" deformations, which are effectively invisible to the alignment algorithms but which produce track parameter biases.

It is important to understand from Monte Carlo studies how various factors, such as misalignment of detector elements, impact physics observables and performance: it will put us in a better position to understand the early collisions data when it arrives, and allows physics analyses to prepare in advance for expected limitations to their measurements.

In this note we investigate the impact of two different types of misalignments of the ATLAS ID and MS systems on tracking performance and the subsequent feed-through to physics and performance:

- Misalignments where the ID module or MS chamber positions have been randomly smeared using Gaussian distributions. Different levels of smearing are used to test the impact of varying degrees of uncertainty in the alignment precision.
- Global systematic misalignments of the Inner Detector. These misalignments cannot be easily removed by the Global χ^2 alignment approach and thus represent potential residual systematic misalignments that could remain even after alignment with a large statistical precision.

[1)] University of Lancaster, Lancaster, UK
[2)] Queen Mary University of London, London, UK
[3)] Laboratori Nazionali di Frascati, INFN, Italy
[4)] Lawrence Berkeley National Laboratory, Berkeley, USA
[5)] University of Wuppertal, Wuppertal, Germany
[6)] University of Bonn, Bonn, Germany
[7)] Tor Vergata University and INFN, Rome, Italy

Table 1: Widths of the Gaussian distributions used to smear the module local x and local y positions for the Day-1 and Day-100 alignment constants

	Day-1 Barrel	Day-1 Endcap	Day-100 Barrel	Day-100 Endcap
Pixel	20 μm	50 μm	10 μm	10 μm
SCT	20 μm	50 μm	10 μm	10 μm
TRT	100 μm	100 μm	50 μm	50 μm

The strategy for investigating the impact of these misalignments is simple. Monte Carlo samples of physics processes are simulated and digitised with a certain ATLAS geometry within which the ID and MS detector elements have a certain position and orientation. However, one can choose which geometry to use in the ATLAS offline event reconstruction of these digitised samples. If one uses exactly the same geometry as the samples were simulated with (the default) then the sample will be reconstructed with "ideal" alignment. If one reconstructs the same digitised event sample using a misaligned ATLAS geometry, one where the module positions/orientations are different to that used in the simulation, one can probe the impact of such misalignments by comparing to the ideal alignment.

This note begins with an explanation and discussion of the Day-1 and Day-100 random ID misalignments and global systematic ID misalignments in Sections 2 and 3 respectively. In Section 3 this includes details on the track reconstruction biases that are introduced by each of the systematic misalignments investigated. The misalignments are then used in Sections 4, 5 and 6 that follow to investigate their impact on $Z \rightarrow \mu\mu$ reconstruction, B-physics observables and Tau performance. In Section 7 the impact of the systematic ID misalignments, as well as random misalignments in the MS, on high-p_T muon reconstruction and Z' analyses are investigated. Finally some overall conclusions to these studies are given in Section 8.

2 Day-1 and Day-100 Misalignments of the Inner Detector

The ID Alignment group has provided two different sets of alignment constants which are intended to represent the expected impact on tracking performance of the ID alignment on the first day and the one hundredth day of data taking. These alignment constants are produced by applying random module level misalignments using a Gaussian distribution centred on zero and with a width as given in Table 1. The module positions are only smeared in the local x and local y directions [1)], and no rotations are introduced. In the case of the TRT, entire TRT modules in the barrel and disks in the endcap have their positions smeared in this way. No attempt is made to introduce global systematic misalignments of the ID. Figures 1 and 2 show the transformations in the Pixel, SCT and TRT global $x-y$ module positions (transverse plane) that are introduced by applying the Day-1 and Day-100 alignment constants. These alignment constants have been entered into the ATLAS conditions database. The conditions database tags that can be used to access the misalignments in ID reconstruction are given in Table 2. Note that there are two different sets of constants that have been entered into the database: which set of constants one should use depends on the exact ATLAS geometry that has been used in the Monte Carlo simulation.

The Gaussian widths used to produce the Day-1 misalignments are determined from the tracking residual distributions in cosmic ray data obtained when the latest alignment constants are used in the

[1)] The axis definitions for the module level uses a local frame where x is in the $r\phi$ direction, y is in the global z direction for barrel and radial direction for endcap modules, and z is out of the module plane.

Table 2: ATLAS COOL database tags for the Day-1 and Day-100 misalignments. The particular tag that should be used is dependent on the geometry used in the simulation.

ATLAS Geometry	Day-1 Tags	Day-100 Tags
Nominal	`InDetSi_Day1-04`	`InDetSi_Day100-04`
	`InDetTRT_Day1-04`	`InDetTRT_Day100-04`
CSC	`InDetSi_CSC_Day1-01`	`InDetSi_CSC_Day100-01`
	`InDetTRT_CSC_Day1-01`	`InDetTRT_CSC_Day100-01`

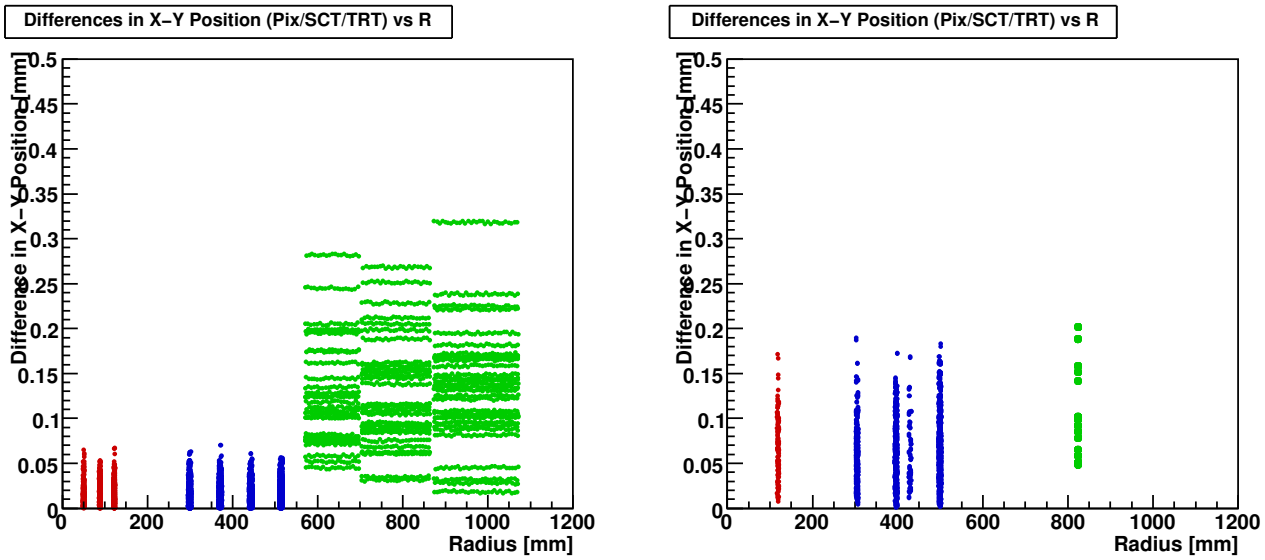

Figure 1: The absolute difference in module global $x-y$ position (transverse plane) as a function of module global radius introduced by the Day-1 alignment constants (Pixel = Red, SCT = Blue, TRT = Green). Left hand plot is for barrel modules, right hand plot for endcap.

reconstruction (database tags `InDet_Cosmic_2008_03` and `TRT_Cosmic_2008_03`). The width is determined by subtracting quadratically the width of the residual distribution in simulated cosmic events with ideal alignment from the width observed in the aligned cosmic data. Due to a lack of track statistics in the endcap regions this operation is only possible in the barrel. For the endcap the widths are increased to reflect the degradation in the alignment performance in this region. Figure 3 shows a reasonable level of agreement between the barrel residual distributions observed in the aligned cosmics data and that which is produced by reconstructing cosmics simulated data with the Day-1 constants.

The Gaussian widths chosen for the Day-100 constants are a best guess of the level of alignment precision that will have been achieved after the alignment algorithms have been run with the statistics available from one hundred days of collisions data. Figure 4 shows that these constants produce residual widths that are intermediate between the current cosmics alignment and the ideal geometry.

When using the Day-1 and Day-100 alignment constants some consideration should also be given as to whether or not the measurement errors require scaling. When we smear module positions randomly we are effectively degrading the hit resolutions, and if the measurement errors are not scaled in order to compensate for this we will see a degradation in fit quality of the tracks: the measurement errors will be

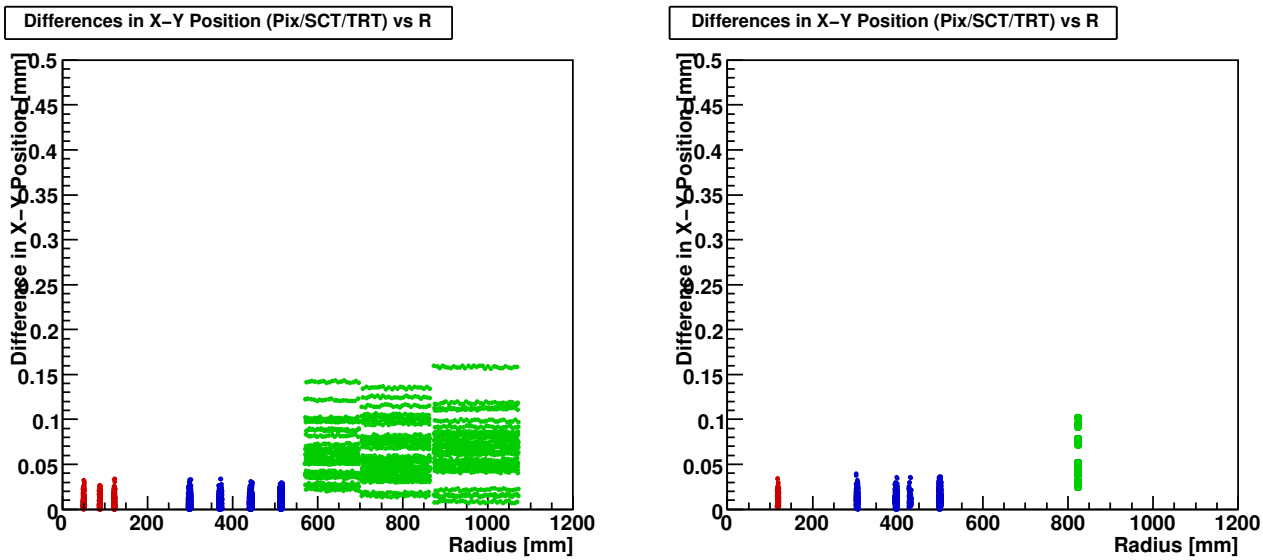

Figure 2: The absolute difference in module global $x-y$ position (transverse plane) as a function of module global radius introduced by the Day-100 alignment constants (Pixel = Red, SCT = Blue, TRT = Green). Left hand plot is for barrel modules, right hand plot for endcap.

underestimated and this could mean that the tracking and vertexing performance will be disproportionately degraded. As such a set of error scaling (ES) constants have been derived for use with the Day-1 and Day-100 alignments, using the methodology described in [3]. These are accessible via the conditions database tags `IndetTrkErrorScaling_Day1-00` and `IndetTrkErrorScaling_Day100-00`. Figure 5(a) shows the χ^2/DOF distribution of tracks ($p_T > 2$ GeV) in a $Z \rightarrow \mu\mu$ sample reconstructed using ideal ID geometry, Day-1 geometry without error scaling and Day-1 with the error scaling applied. The results for the Day-100 geometry are shown in Figure 5(b). One can see that in both cases when the error scaling is applied we obtain a χ^2/DOF distribution that is compatible with that of the ideal geometry. Note that since error scaling doesn't rely on any prior knowledge of the alignment of the Inner Detector it is realistic to apply this.

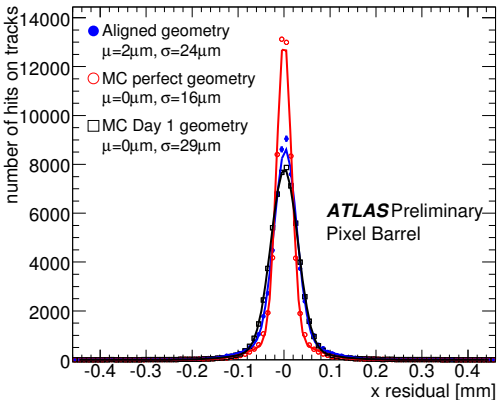

(a) Pixel Barrel Residual X.

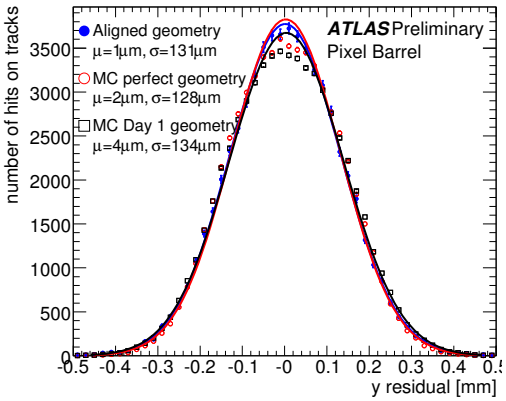

(b) Pixel Barrel Residual Y.

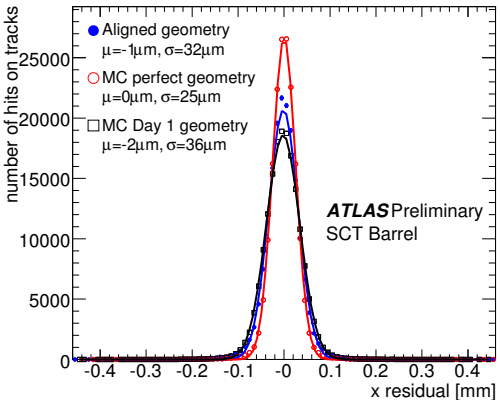

(c) SCT Barrel Residual X.

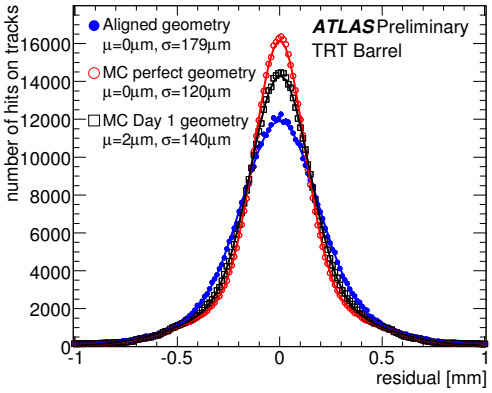

(d) TRT Barrel Residual.

Figure 3: A comparison of ID barrel tracking residual distributions between cosmics simulation reconstructed with ideal alignment, cosmics simulation reconstructed with the Day-1 alignment constants and cosmics data reconstructed using the `InDet_Cosmic_2008_03` database tags.

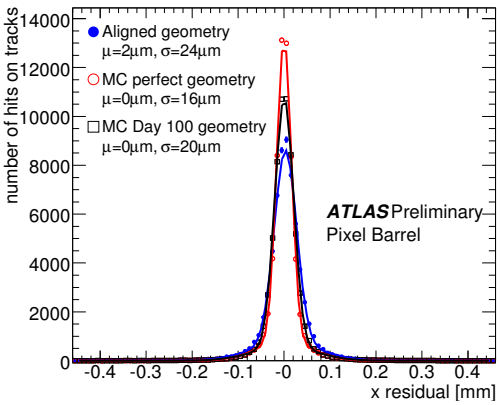

(a) Pixel Barrel Residual X.

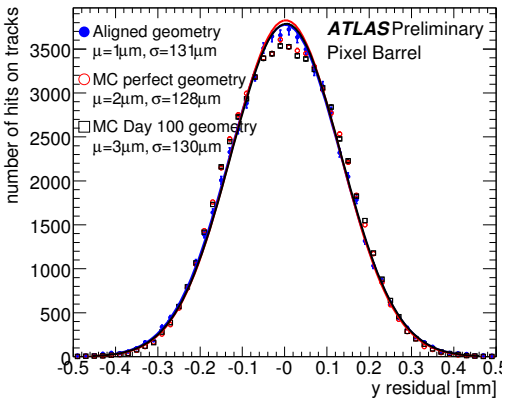

(b) Pixel Barrel Residual Y.

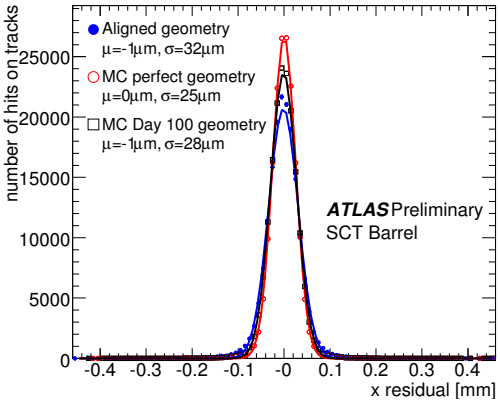

(c) SCT Barrel Residual X.

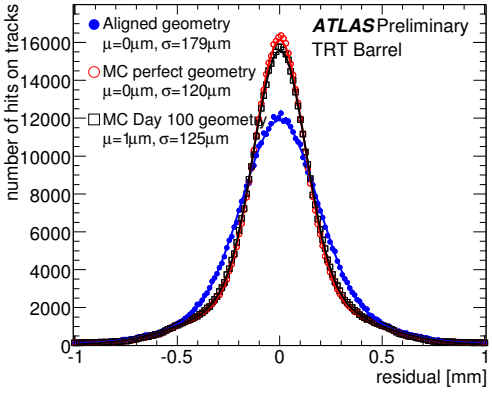

(d) TRT Barrel Residual.

Figure 4: A comparison of ID barrel tracking residual distributions between ideal cosmics simulation, Day-100 cosmics simulation and cosmics data.

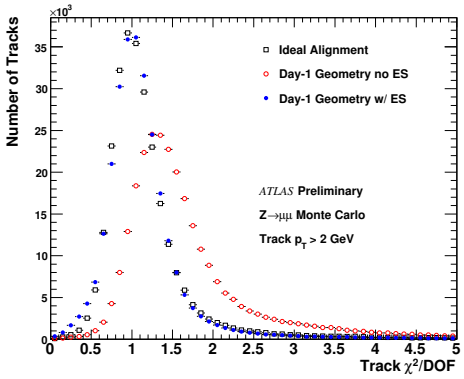

(a) χ^2/DOF distribution for ideal, Day-1 with ES and Day-1 without ES alignment .

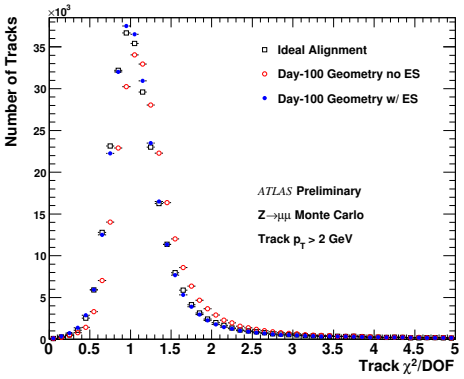

(b) χ^2/DOF distribution for ideal, Day-100 with ES and Day-100 without ES alignment.

Figure 5: Impact of error scaling on χ^2/DOFdistributions of tracks in a simulated $Z \rightarrow \mu\mu$ sample reconstructed using Day-1 and Day-100 geometries.

3 Global Systematic Misalignments of the Inner Detector

Unlike random module-to-module misalignments, global systematic misalignments of large scale structures, such as rotations/translations of entire barrel layers or endcap disks, have the potential to introduce systematic biases in the track reconstruction. Clearly there are many such global systematic misalignments that could potentially be present in the ATLAS Inner Detector structure. The vast majority of these will produce biases in the tracking residuals and can thus be removed by the ID alignment algorithms.

However, there exist a number of global systematic misalignments which, for tracks originating at a common interaction point, leave the tracking residuals unbiased (within the measurement accuracy). With certain initial conditions it is thus possible that alignment approaches which rely on the minimisation of tracking residuals could converge on such a misalignment, known as a "weak mode" misalignment. In this situation one would not know from an examination of tracking residuals that the detector was in fact misaligned. Several approaches to tackle weak mode misalignments are being investigated, such as running the alignment algorithms using a track sample with a different topology (cosmic ray, beam gas or beam halo tracks), or using additional constraints in the alignment algorithms: calorimetry measurements, the reconstructed primary vertex or track pairs from J/ψ and Z decays.

Unfortunately we cannot know a priori to which weak mode misalignments we may be susceptible or how large these misalignments could be. However, in order to facilitate an understanding of which weak modes may have the greatest impact on ID tracking, and how we might remove them, we have attempted to create several weak mode misalignments of the ATLAS Inner Detector "by hand". These are described in detail in [5]. Global systematic misalignments produced via transformations of module global R (radius), ϕ or z coordinates $(\Delta R, \Delta\phi, \Delta z)$ as a function of module R, ϕ or z, have the property of retaining approximate helical trajectories for particles originating at the interaction point [4]. Thus far the following misalignments produced in this way have been considered:

- The Curl misalignment $\Delta\phi = c_1 R + c_2/R$: A transformation of module global ϕ coordinates with magnitude dependent on the module radius.
- The Twist misalignment $\Delta\phi = cz$: A transformation of module global ϕ coordinates with magnitude dependent on the module global z coordinate [2)].
- The Telescope misalignment $\Delta z = cR$: A transformation of module global z coordinates with magnitude dependent on the module radius.
- The Elliptical misalignment $\Delta R = c\frac{1}{2}\cos(2\phi)R$: A transformation of module global R coordinates with magnitude dependent on the module global ϕ. The effect of this parameterisation is to radially expand the top and bottom half of the ID whilst radially contracting the sides.

The simple parameterisations of the misalignments described above should result in weak mode misalignments, but only if each measurement on a track can be freely translated and rotated in the global frame. We know that in reality this is not possible. Each measurement is necessarily constrained to be on a detector element, and it is only the detector element that can be transformed and rotated, not the measurement itself. For example, a perfect Curl misalignment should have each measurement rotated in global ϕ by an amount proportional to the radial distance from the beampipe. However, this radial distance is clearly not the same for each measurement on an endcap detector element, and even in the

[2)] The implementation of the Twist misalignment in the TRT barrel has to be modified since the modules span the entire length of the barrel. Instead the TRT modules are rotated about an axis that points radially out from the interaction point through the centre of the module

barrel a small difference in the radial distance across the detector elements exists. Thus misalignments generated using these simple parameterisations are likely only to approximate weak modes.

Two magnitudes of misalignment are studied for each of the above types, labelled "Large" and "Small". The constants of proportionality for the Curl-Large and Twist-Large misalignments are chosen such that modules in the outermost SCT layer are translated in the azimuthal plane by $\sim 300\ \mu$m. The $1/R$ term in the Curl parameterisation produces a $\sim 50\ \mu$m shift of modules in the innermost pixel layer. The Telescope-Large and Telescope-Small misalignments produce Δz translations of the outermost SCT layer of $\sim 3000\ \mu$m and $\sim 300\ \mu$m respectively, and the Elliptical-Large and Elliptical-Small misalignments correspond to radial shifts of $\sim 1000\ \mu$m and $\sim 250\ \mu$m respectively. No random module-to-module misalignments are introduced in any of the parameterised global deformations. It should be noted that the choice for the magnitude of these misalignments is somewhat arbitrary, and motivated by the desire for misalignments large enough to have some visible impact on track reconstruction. Currently we have only a limited understanding of the size of weak mode misalignments that we could encounter in the real detector. Thus any impact on physics and performance that is observed using these misalignments should be interpreted as being indicative of possible effects.

The Curl-Small and Twist-Small misalignments are produced by running the Global χ^2 alignment algorithm [6] on an ID geometry that has been misaligned using the Curl-Large and Twist-Large misalignments respectively. A sample of simulated muon tracks with $2 < p_T < 50$ GeV and a common interaction point were used for the alignment. The exact alignment procedure used is detailed in [5], and closely approximates that used in the 'CSC Alignment Exercise' [7], with the exception that no cosmic ray events were used in the alignment. It should also be noted that a rather limited number of tracks were used in the alignment of the TRT barrel and Pixel and SCT endcaps, and that the TRT endcaps were not aligned at all (due to the limitations of the TRT alignment algorithm at the time of producing these misalignments). Thus we expect that these alignments could be improved considerably.

In this section we highlight the track reconstruction biases that are introduced by each of the global systematic misalignments. Further plots can be found in [5]. A sample of 60000 CSC simulated $Z \rightarrow \mu\mu$ events [3)] have been reconstructed with InDetRecExample in release 14.5.1. Different ID geometries are used in the reconstruction. Ideal alignment corresponds to using the same geometry in the reconstruction as that used in the simulation (`ATLAS-CSC-01-02-00`). To reconstruct with a misaligned weak mode geometry we reconstruct using the appropriate conditions database tag as described in Section 4 of [5]. All plots are made using Inner Detector reconstructed tracks requiring $p_T > 2$ GeV (no track quality requirements are made, but we are interested in biases and not resolutions here). The reconstructed p_T and η spectra of these tracks are shown in Figure 6, when reconstructed with ideal alignment and Curl misalignments. Some differences in the p_T spectra are clearly evident between the Curl-Large and ideal geometries.

In Figure 7 is shown the track χ^2/DOF distribution. For all systematic misalignments with the exception of the Elliptical-Large the χ^2/DOF distribution agrees well with that achieved using ideal alignment in the track reconstruction, thus demonstrating that these misalignments are reasonable approximations to weak modes[4)]. This is further evidenced by the track residual distributions presented in [5]. The χ^2/DOF distribution produced by the Elliptical-Large misalignment indicates that the size of the radial transformations introduced here are too large to approximate a weak mode misalignment. A χ^2-based alignment approach should be able to remove or substantially reduce an Elliptical misalignment of this size.

[3)] misal1_mc12.005151.McAtNloZmumu.digit.RDO.v12003108

[4)] Here we have only considered track topologies produced in simulated beam collisions, thus this does not demonstrate that these misalignments approximate weak modes to other track topologies such as cosmic rays or beam halo events. It is possible that these misalignments could be reduced by running the alignment algorithms with such events.

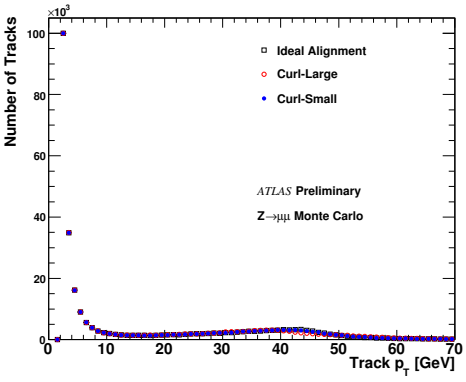

(a) Reconstructed Track p_T.

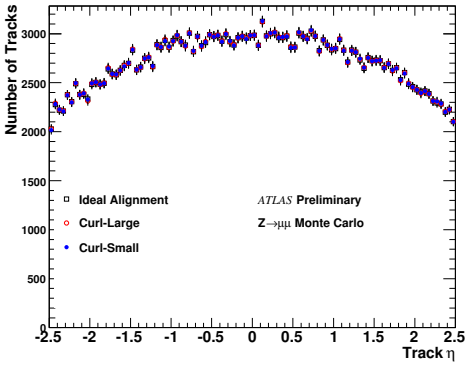

(b) Reconstructed Track η (ID fiducial coverage $|\eta| < 2.5$).

Figure 6: Track p_T and η spectra for the tracks in the $Z \rightarrow \mu\mu$ sample, reconstructed with ideal and Curl misaligned ID geometries.

In order to probe the biases in track reconstruction introduced by the systematic misalignments we compare the reconstructed track parameters to those of the true particle track at perigee. This is done by using the `TrackTruthCollection` to retrieve the HepMC particle that best matches to the reconstructed track, and then using the `TruthToTrackTool` to generate the perigee parameters for that HepMC particle. In Figure 8 we see the difference between the true and reconstructed d_0 and Q/p_T tracking parameters where the tracks have been reconstructed using the Curl-Large, Curl-Small and ideal ID geometries. One can see that the Curl-Large misalignment produces a bias in the curvature of $\Delta Q/p_T \sim -0.002$. Positively charged tracks will have their curvature reduced by approximately this amount, and negatively charged tracks their curvature increased. The Curl-Small misalignment produces a much smaller curvature bias of $\Delta Q/p_T \sim -0.0004$, demonstrating the success of the ID alignment in correcting for this misalignment, and therefore that the Curl-Large is only an approximation to a weak mode. By using a larger number of tracks in the alignment, and in particular different track topologies such as those found in cosmic ray and beam halo events, it is likely that the curvature bias could be reduced even further. The impact of these curvature biases on the reconstructed track p_T can be seen in Figure 9. At $p_T = 50$ GeV the reconstructed track p_T is biased by $\sim 12\%(\sim 2\%)$ in the Curl-Large(Curl-Small) cases, and the bias is correspondingly positive(negative) for positively(negatively) charged tracks. The bias is larger in the case of the positively charged tracks. This is because of the non-linear effect on the measured transverse momentum produced by a variation in track curvature[5)].

The Curl-Large misalignment also produces a $\sim 50\,\mu$m bias in the reconstructed impact parameter d_0 of the tracks, which is not present in the Curl-Small geometry. This bias is introduced by the $1/R$ term in the original Curl parameterisation [5], but since the alignment is performed using a soft constraint to the (known) beamline position of (0,0) in the $x-y$ plane this bias is naturally removed in the aligned Curl-Small geometry.

In Figure 10 is shown the track curvature biases introduced by the Twist-Large and Twist-Small

[5)]To further illustrate this consider a Curl misalignment which produces a curvature bias of $\Delta Q/p_T = -0.02$. A track of true $p_T = 50$ GeV will be reconstructed with infinite momenta if it is positively charged, but reconstructed with $p_T = 25$ GeV if it is negatively charged.

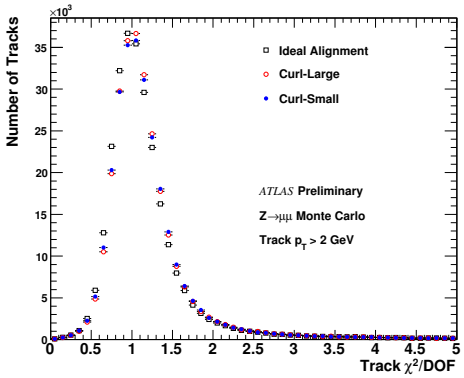

(a) Tracks χ^2/DOF distribution for Curl deformations.

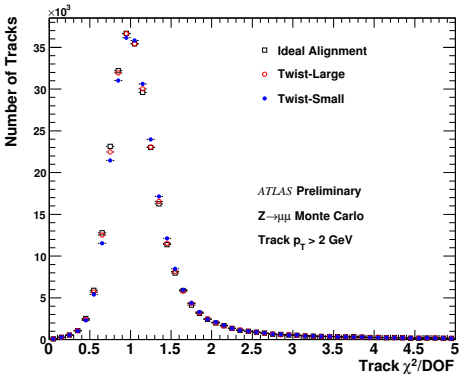

(b) Tracks χ^2/DOF distribution for Twist deformations.

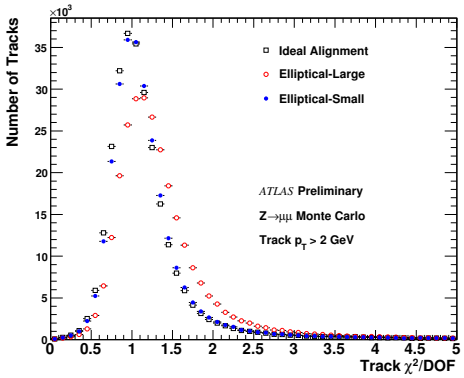

(c) Tracks χ^2/DOF distribution for Elliptical deformations.

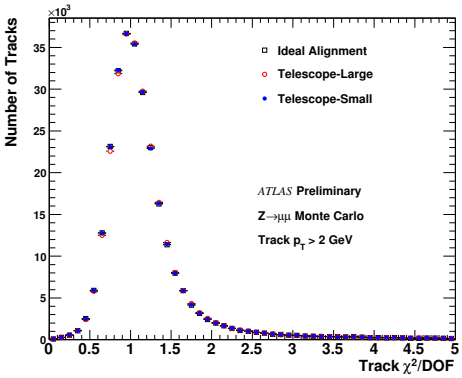

(d) Tracks χ^2/DOF distribution for Telescope deformations.

Figure 7: χ^2/DOF distributions of Inner Detector tracks for each of the different systematic misalignments compared to the ideal alignment case.

misalignments. The Twist misalignment produces a detector-η dependent curvature bias. In the barrel region (Figure 10(a)) we see a degradation in the curvature resolution since the twist is in opposite directions on the positive/negative detector-η sides of the barrel. The curvature bias acts in opposite directions in the two endcaps as expected from the parameterisation of the misalignment (Figures 10(b) and 10(c)). In Figure 11 we see the impact of these curvature biases on the reconstructed track p_T for the different detector regions. As expected no p_T-bias is observed when integrating over the barrel. In Endcap A at $p_T = 50$ GeV the reconstructed track p_T is biased by $\sim 20\%$ for positively charged tracks, with a smaller $\sim 12\%$ bias for negatively charged tracks. The situation is reversed in Endcap C due to the opposite sign of the curvature bias here. Figure 11 also shows very little difference between the p_T-bias of the Twist-Large and Twist-Small geometry: this is because only the Pixel and SCT detectors have been aligned in the Twist-Small misalignment. The TRT endcap has not been aligned, and thus this limits the extent to which the alignment can improve the situation for tracks which are reconstructed using TRT hits.

In Figure 12 is shown the track η bias introduced by the Telescope-Large and Telescope-Small misalignments. Even for the extreme Telescope-Large misalignment case this bias is rather small. The bias is itself η dependent. This is understood to be due to the inherent incompatibility between the endcap construction and an ideal Telescope misalignment, as explained in Section 3.3 of [5].

In Figure 13 is shown the impact on the track η and z_0 parameters produced by the Elliptical-Large and Elliptical-Small misalignments. A considerably larger impact is observed for the larger Elliptical-Large misalignment. Here the resolutions of the η and z_0 track parameters is clearly degraded with respect to the ideal alignment case. As expected the impact is much larger in the endcaps: a radial shift in hits on a track will produce a larger impact on reconstructed η and z_0 at large η than at small η.

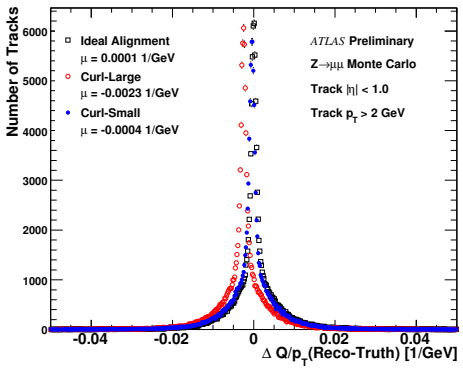

(a) Barrel curvature bias for Curl misalignments (track $|\eta| < 1.0$).

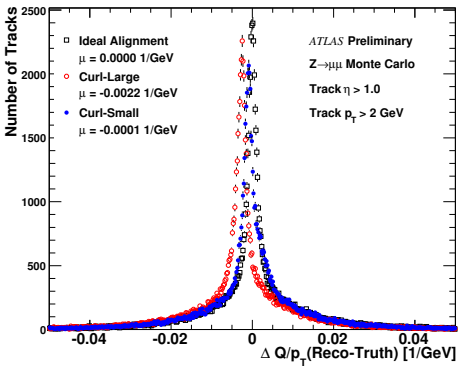

(b) Endcap A curvature bias for Curl misalignment (track $\eta > 1.0$).

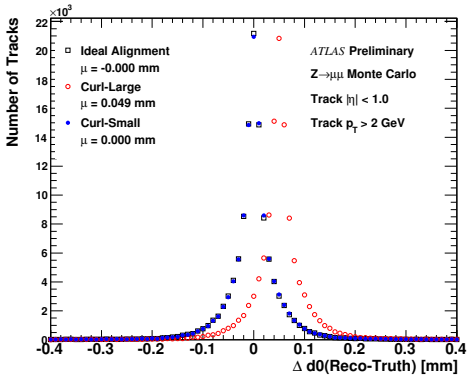

(c) Barrel d_0 bias for Curl misalignment (track $|\eta| < 1.0$).

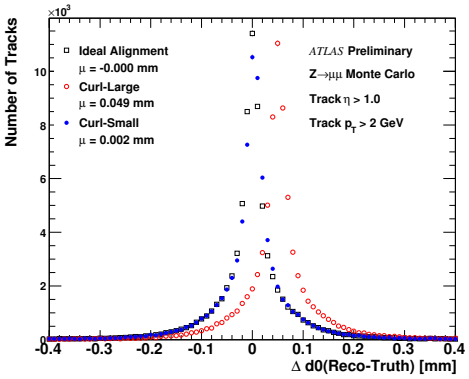

(d) Endcap A d_0 bias for Curl misalignment (track $\eta > 1.0$).

Figure 8: d_0 and curvature track parameter biases introduced by the Curl-Large and Curl-Small misalignments in barrel and endcap regions.

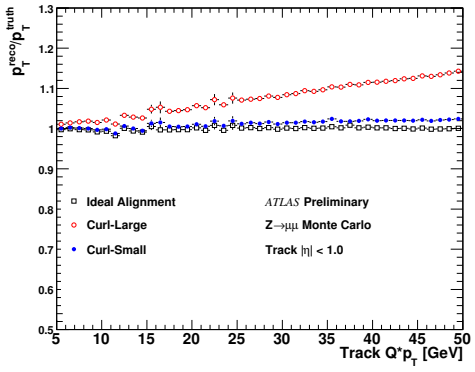

(a) Barrel positive track p_T-bias for Curl misalignment (track $|\eta| < 1.0$).

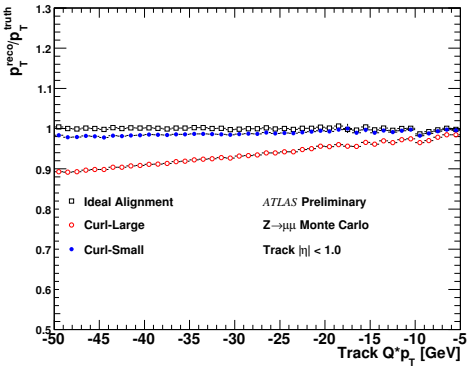

(b) Barrel negative track p_T-bias for Curl misalignment (track $|\eta| < 1.0$).

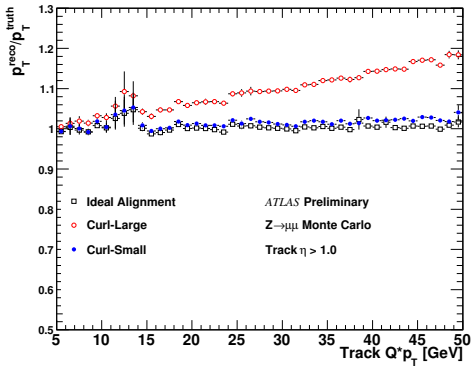

(c) Endcap A positive track p_T-bias for Curl misalignment (track $\eta > 1.0$).

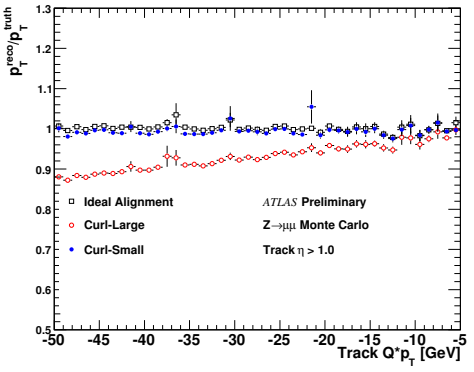

(d) Endcap A negative track p_T-bias for Curl misalignment (track $\eta > 1.0$).

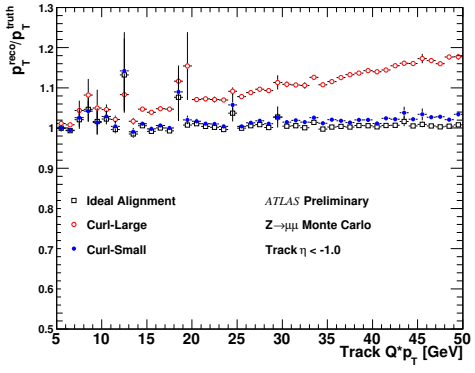

(e) Endcap C positive track p_T-bias for Curl misalignment (track $\eta < -1.0$).

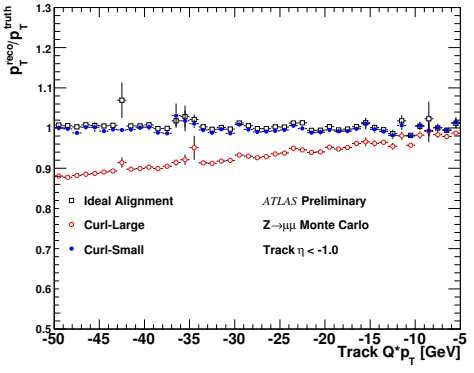

(f) Endcap C negative track p_T-bias for Curl misalignment (track $\eta < -1.0$).

Figure 9: Reconstructed track p_T-bias introduced by the Curl-Large and Curl-Small misalignments in the barrel and endcap regions. The points correspond to the statistical mean in that bin, and the error shown is the statistical error on this mean. Anomolous points with large error bars are caused by outliers.

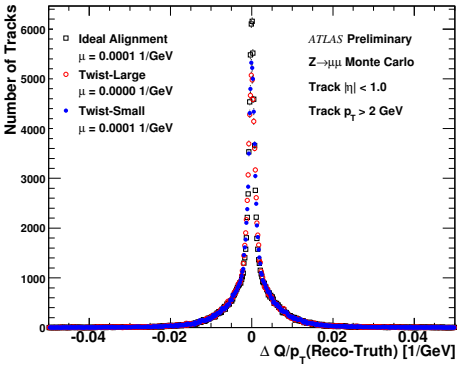

(a) Barrel curvature bias for Twist misalignment (track $|\eta| < 1.0$).

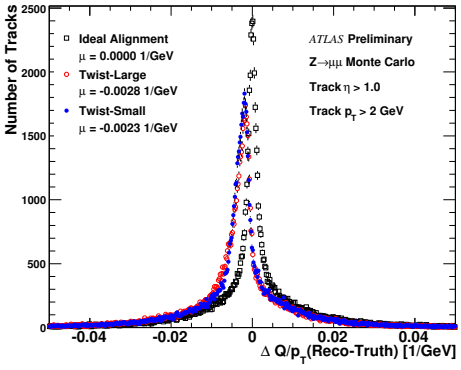

(b) Endcap A curvature bias for Twist misalignment (track $\eta > 1.0$).

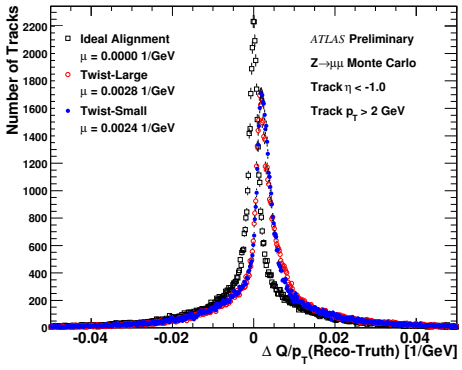

(c) Endcap C curvature bias for Twist misalignment (track $\eta < -1.0$).

Figure 10: Curvature biases introduced by the Twist-Large and Twist-Small misalignments in the barrel and endcap regions.

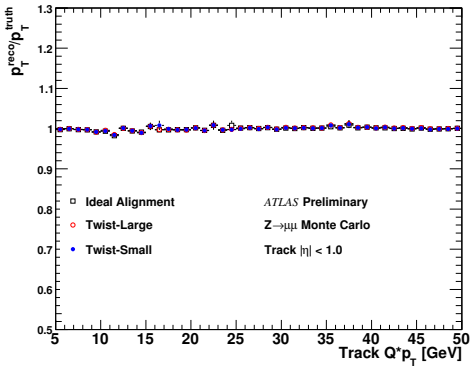

(a) Barrel positive track p_T-bias for Twist misalignment (track $|\eta| < 1.0$).

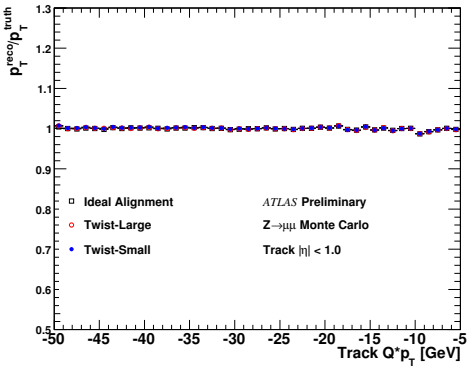

(b) Barrel negative track p_T-bias for Twist misalignment (track $|\eta| < 1.0$).

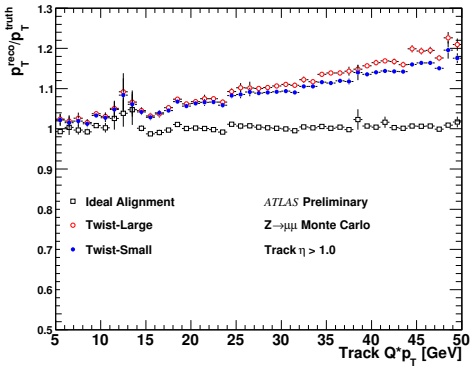

(c) Endcap A positive track p_T-bias for Twist misalignment (track $\eta > 1.0$).

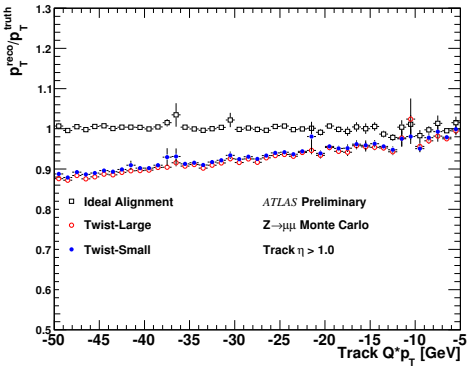

(d) Endcap A negative track p_T-bias for Twist misalignment (track $\eta > 1.0$).

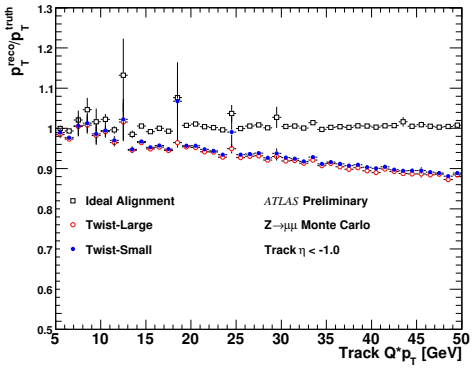

(e) Endcap C positive track p_T-bias for Twist misalignment (track $\eta < -1.0$).

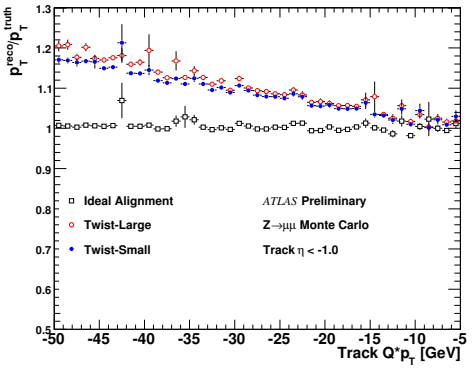

(f) Endcap C negative track p_T-bias for Twist misalignment (track $\eta < -1.0$).

Figure 11: Reconstructed track p_T-bias introduced by the Twist-Large and Twist-Small misalignments in the barrel and endcap regions. The points correspond to the statistical mean in that bin, and the error shown is the statistical error on this mean. Anomolous points with large error bars are caused by outliers.

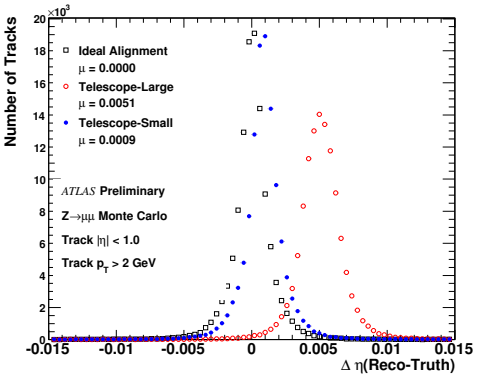

(a) Barrel η bias for Telescope misalignment (track $|\eta| < 1.0$).

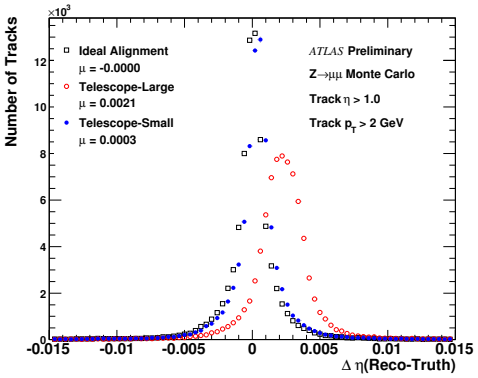

(b) Endcap A η bias for Telescope misalignment (track $\eta > 1.0$).

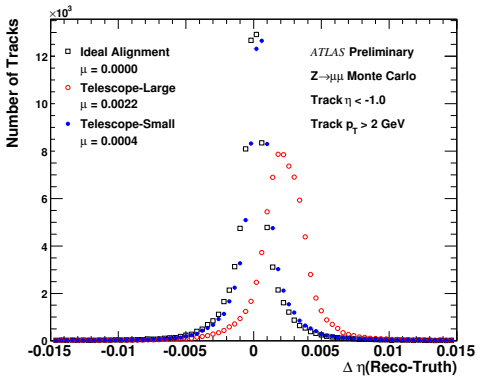

(c) Endcap C η bias for Telescope misalignment (track $\eta < -1.0$).

Figure 12: Track η parameter biases introduced by the Telescope-Large and Telescope-Small misalignments in the barrel and endcap regions.

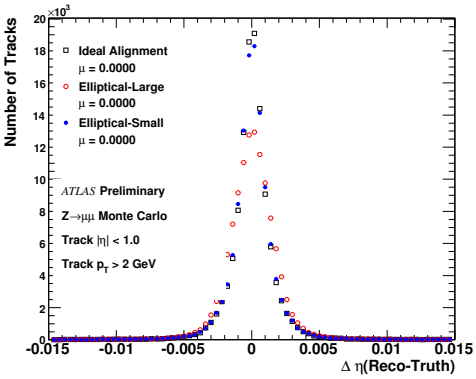

(a) Barrel η bias for Elliptical misalignment (track $|\eta| < 1.0$).

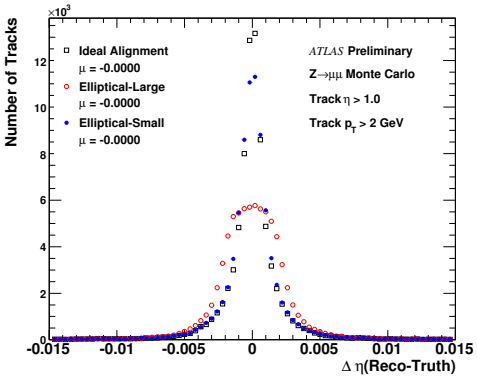

(b) Endcap A η bias for Elliptical misalignment (track $\eta > 1.0$).

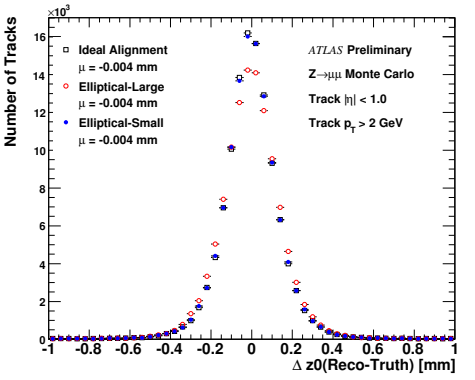

(c) Barrel z_0 bias for Elliptical misalignment (track $|\eta| < 1.0$).

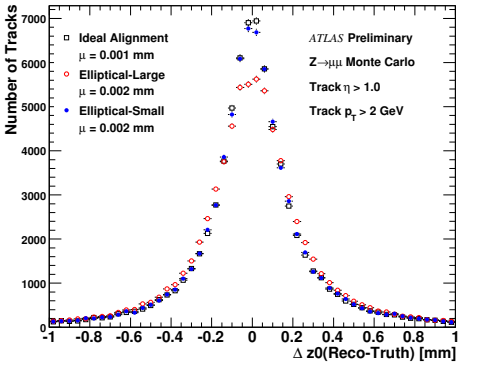

(d) Endcap A z_0 bias for Elliptical misalignment (track $\eta > 1.0$).

Figure 13: Track η and z_0 parameter biases introduced by the Elliptical-Large and Elliptical-Small misalignments in the barrel and endcap regions.

4 Impact of Misalignments on Z Boson Reconstruction

In this section we examine the impact of misalignments of the ATLAS Inner Detector on the reconstruction of $Z \rightarrow \mu\mu$ events. Two different types of misalignments are investigated; the Day-1/Day-100 random misalignments described in Section 2 and the global systematic misalignments described in Section 3.

For these studies a sample of 60000 CSC simulated $Z \rightarrow \mu\mu$ events [6] have been reconstructed in release 14.5.1, using different conditions database tags corresponding to the different geometries to override the Inner Detector pixel, SCT and TRT module positions. We follow here exactly the same methodology as described in Section 4 of [5]. The same event sample with otherwise identical reconstruction is always used such that any differences observed are due to changes in the ID module positions only. The p_T and η spectra of the tracks in this sample are shown in Figure 6.

4.1 Impact of Global Systematic Misalignments on Inner Detector Reconstructed Z Mass

In Section 3 the size and type of track reconstruction biases produced by each of the Curl, Twist, Elliptical and Telescope systematic misalignments were shown. In this section we investigate how these biases impact on the reconstruction of the Z boson mass using Inner Detector tracks. Since we use a pure $Z \rightarrow \mu\mu$ sample without any background processes present this can be tested with very simple Z boson identification criteria.

The mass of the Z boson is reconstructed by calculating the invariant mass formed from the two highest-p_T Inner Detector tracks, with both tracks satisfying $p_T > 15$ GeV and having opposite charge. In Figures 14 is shown the Z mass for events reconstructed using the ideal geometry and for each systematic misalignment studied. In Figures 15, 16, 17 and 18 is shown for each misalignment the event-by-event difference between the Z mass as reconstructed from the ID tracks and the Z mass as reconstructed from the two matching truth particle tracks (using the same truth matching as described in Section 3). Each figure displays two distributions, one where every reconstructed Z event is plotted, and the other only where both tracks satisfy $|\eta| < 1.0$. These distributions are fitted with a Gaussian function in the range $[\mu - \sigma_{RMS}, \mu + \sigma_{RMS}]$, and the mean and width of this Gaussian stated in the plot.

In Figures 15 and 16 we can see that the charge-dependent p_T-biases produced by the Curl and Twist systematic misalignments have the effect of degrading the Z mass resolution. The degradation in the mass resolution is $\sim 30\%$($\sim 20\%$) in the Curl-Large(Curl-Small) cases, which becomes $\sim 38\%$($\sim 9\%$) if both legs are required to have $|\eta| < 1.0$. The improvement in using the Curl-Small compared with the Curl-Large geometry is a consequence of the alignment procedure being able to remove the p_T-bias of the Curl misalignment to a large extent, as was earlier evidenced by Figure 9. However, whereas the p_T-bias is substantially smaller in the Curl-Small case, the improvement in the Z mass resolution is not so dramatic. The reason for this is that, due to the limited statistics used, the alignment algorithm produces residual random misalignments in the TRT barrel and SCT endcap detector modules which subsequently degrade the tracking resolutions. In reality, with collision data, such statistical uncertainties will be rapidly reduced. In Figure 15 one can also see that the Curl-Large misalignment introduces a ~ 400 MeV bias into the reconstruction of the Z mass. This is a consequence of the positive p_T-bias for positively charged tracks being slightly larger than the negative p_T-bias for negatively charged tracks (see Figure 9).

The degradation in the mass resolution is more extreme in the case of the Twist misalignments, more than doubling in both the Twist-Large and Twist-Small cases when no η restrictions are applied to the tracks. This is because, as can be seen from Figures 10(b), 10(c) and 11, the curvature and hence

[6] misal1_mc12.005151.McAtNloZmumu.digit.RDO.v12003108

p_T-bias of the Twist misalignments is larger than in the Curl case. Although a marginal improvement was seen in the p_T-bias of the tracks when using the Twist-Small misalignment compared with the Twist-Large(Figure 11), this is not significant enough to improve the Z mass resolution. The Twist misalignments do not produce a bias in the reconstructed Z mass because when integrated across the whole Inner Detector there is no net curvature bias (the curvature bias being in opposite directions in the A and C sides).

A degradation in the Z mass resolution of $\sim 20\%$ is observed for the Elliptical-Large misalignment. This is likely due simply to the degradation in track fit quality that occurs when using this misalignment, as seen in Figure 7(c). Thus these results have to be viewed in light of the fact that it is likely the ID alignment procedure could use these very same degradations in track fit quality to correct for the Elliptical misalignment. The Elliptical-Small misalignment, which does not result in poorer track fits, does not produce an impact on the Z mass reconstruction.

No impact on the Z mass reconstruction is observable for the Telescope-Large or Telescope-Small misalignments. This is not surprising since these misalignments only produce a very small bias in the reconstructed track η. Since this bias itself has some track η-dependence it could conceivably impact on the opening angle of the two-leg Z decay but the affect is not large enough to be visible.

4.2 Impact of Day-1 and Day-100 Random Misalignments on Inner Detector Reconstructed Z Mass

In this section we investigate what impact the Day-1 and Day-100 Inner Detector misalignments (Section 2) have on the Z mass reconstructed using Inner Detector tracks. We use the same $Z \rightarrow \mu\mu$ sample and the same Z mass reconstruction as described in the previous section. The Day-1 geometry is implemented in the reconstruction via the conditions database tags `InDetSi_CSC_Day1-01` and `InDetTRT_CSC_Day1-01`, and the Day-100 via `InDetSi_CSC_Day100-01` and `InDetTRT_CSC_Day100-01`[7]. In addition we also use the corresponding conditions database tags to implement the scaling of the Inner Detector measurement errors as described in Section 2.

Figure 19 compares the Z mass when tracks are reconstructed using the ideal geometry to the Z mass when tracks are reconstructed with the Day-1 and Day-100 misalignments. Figure 20 shows the event-by-event difference between the Z mass as reconstructed from the ID tracks and the Z mass as reconstructed from the two matching truth particle tracks as described in the previous section. The impact of the random misalignments on the Z mass resolution is significant. The Day-1 geometry degrades the Z mass resolution by $\sim 50\%$. The Day-100 geometry uses reduced Gaussian widths to smear the module positions, and consequently the impact on the Z mass resolution is smaller, a $\sim 13\%$ degradation.

4.2.1 Impact of Error Scaling

In order to investigate the impact of scaling the measurement errors the Z mass reconstruction was performed using tracks reconstructed with the Day-1 and Day-100 geometries but without the error scaling applied. Figure 21 shows the impact on the Z mass resolution of the error scaling in the Day-1 and Day-100 cases. One can see that the impact of the error scaling is negligible here.

[7] These database tags correspond to the alignments which implement the Day-1 and Day-100 geometries on top of the CSC misaligned geometry, which is what was used in the simulation of this $Z \rightarrow \mu\mu$ sample.

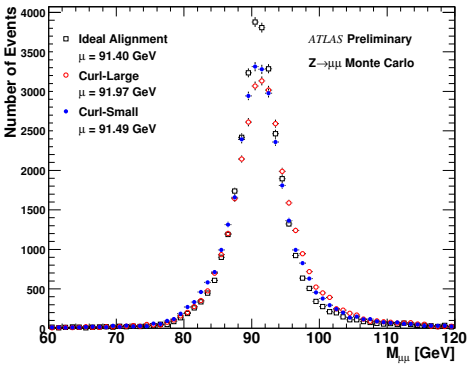

(a) Curl-Large and Curl-Small misalignments.

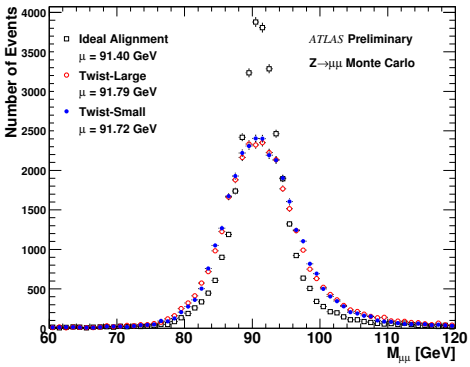

(b) Twist-Large and Twist-Small misalignments.

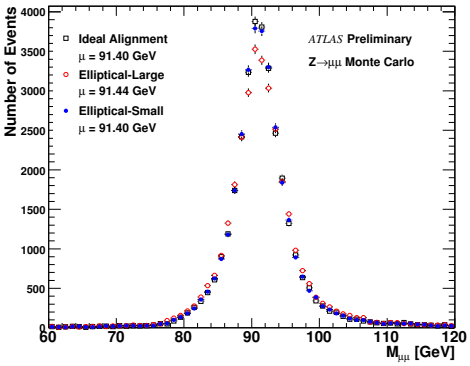

(c) Elliptical-Large and Elliptical-Small misalignments.

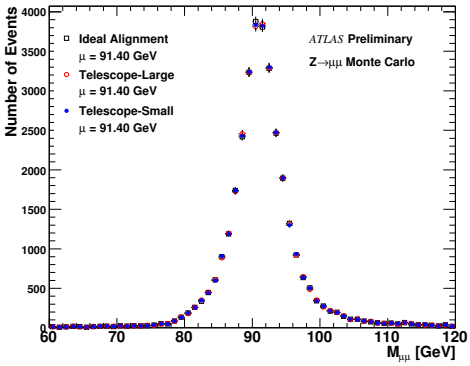

(d) Telescope-Large and Telescope-Small misalignments.

Figure 14: Reconstructed Z mass for each of the systematic misalignment cases studied, compared with that of the ideal alignment case.

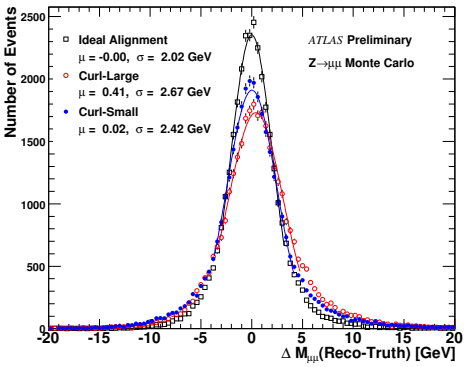

(a) $\Delta M_{\mu\mu}(\text{Reco} - \text{Truth})$ no η restriction.

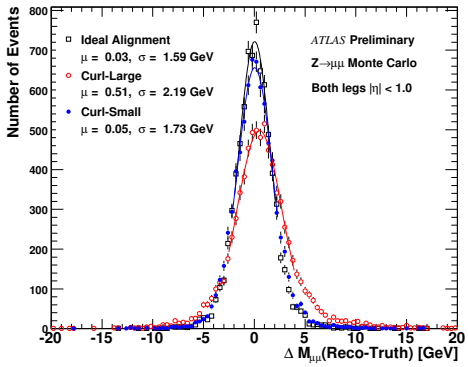

(b) $\Delta M_{\mu\mu}(\text{Reco} - \text{Truth})$ requiring both legs $|\eta| < 1.0$.

Figure 15: Impact of Curl-Large and Curl-Small misalignment on Z mass resolution.

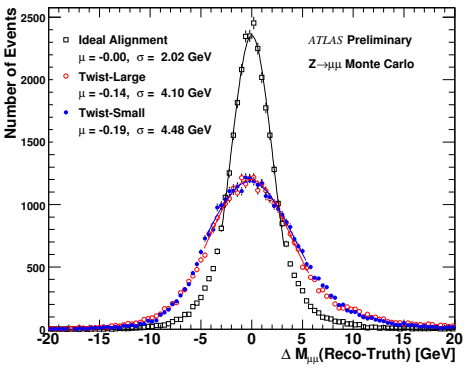

(a) $\Delta M_{\mu\mu}(\text{Reco} - \text{Truth})$ no η restriction.

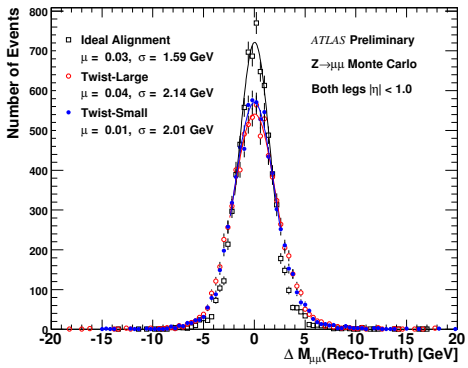

(b) $\Delta M_{\mu\mu}(\text{Reco} - \text{Truth})$ requiring both legs $|\eta| < 1.0$.

Figure 16: Impact of Twist-Large and Twist-Small misalignment on Z mass resolution.

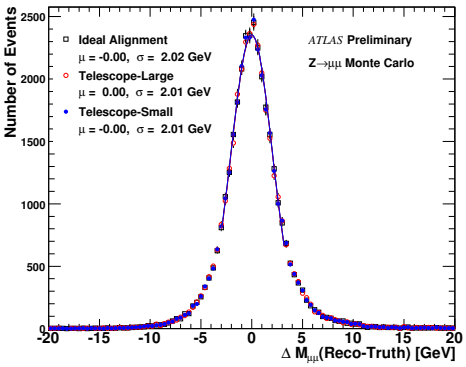

(a) $\Delta M_{\mu\mu}(\text{Reco} - \text{Truth})$ no η restriction.

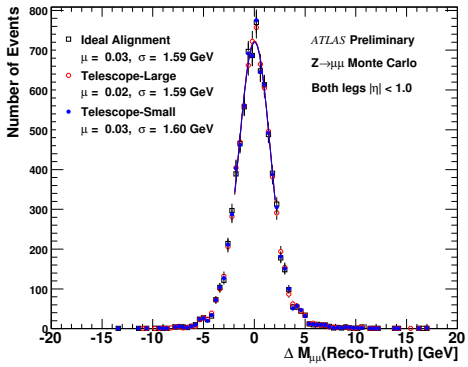

(b) $\Delta M_{\mu\mu}(\text{Reco} - \text{Truth})$ requiring both legs $|\eta| < 1.0$.

Figure 17: Impact of Telescope-Large and Telescope-Small misalignment on Z mass resolution.

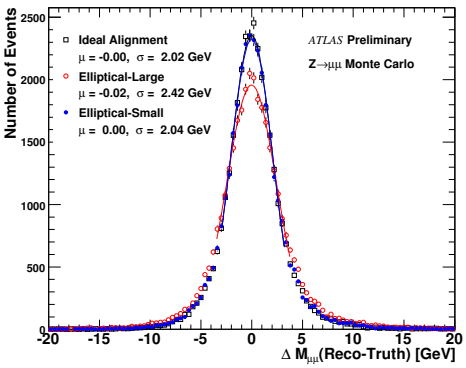

(a) $\Delta M_{\mu\mu}(\text{Reco} - \text{Truth})$ no η restriction.

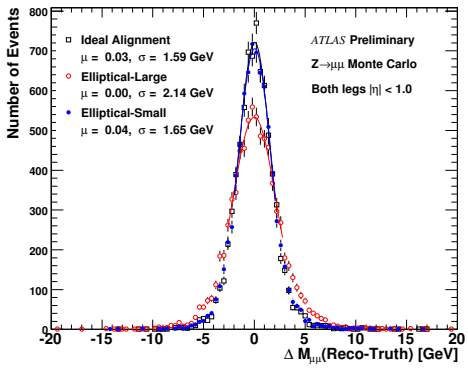

(b) $\Delta M_{\mu\mu}(\text{Reco} - \text{Truth})$ requiring both legs $|\eta| < 1.0$.

Figure 18: Impact of Elliptical-Large and Elliptical-Small misalignment on Z mass resolution.

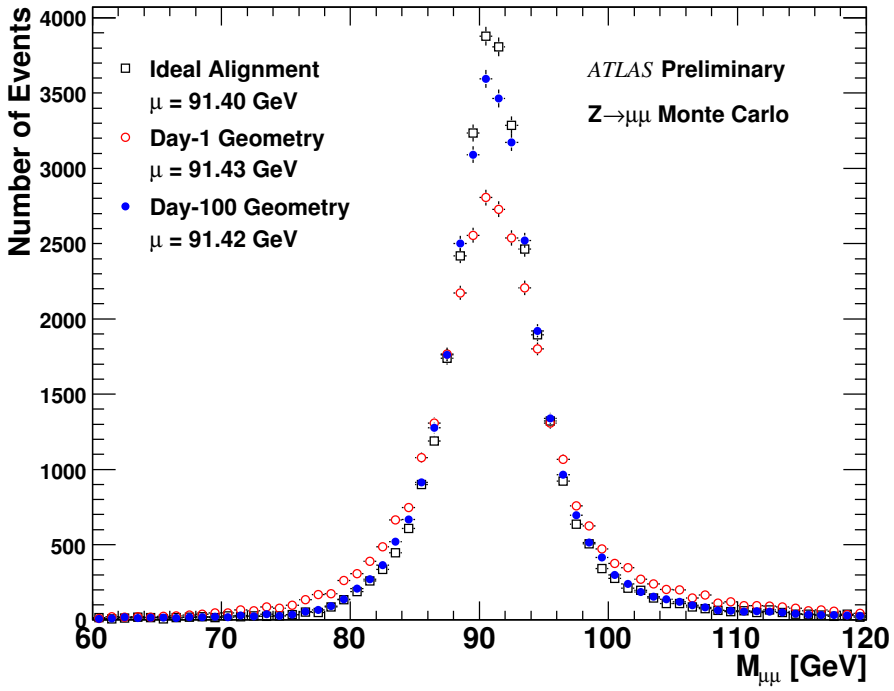

Figure 19: Reconstructed Z mass using the Day-1 and Day-100 geometries, compared with that of the ideal geometry case.

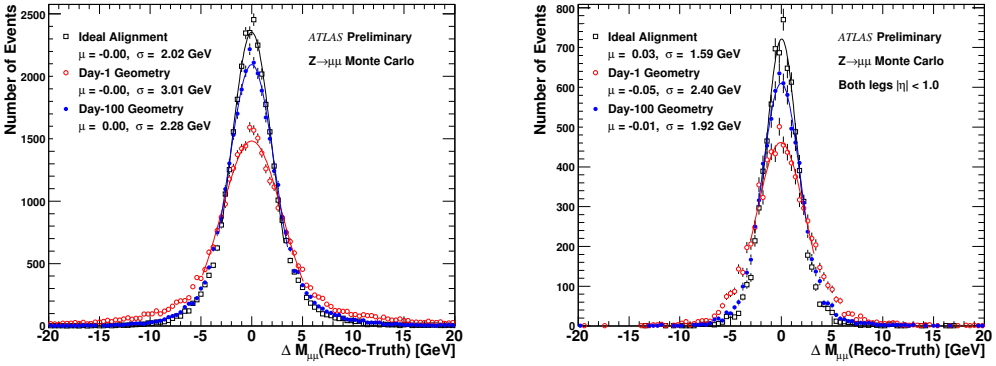

(a) $\Delta M_{\mu\mu}(\text{Reco} - \text{Truth})$ no η restriction.

(b) $\Delta M_{\mu\mu}(\text{Reco} - \text{Truth})$ requiring both legs $|\eta| < 1.0$.

Figure 20: Impact of Day-1 and Day-100 misalignments on Z mass resolution.

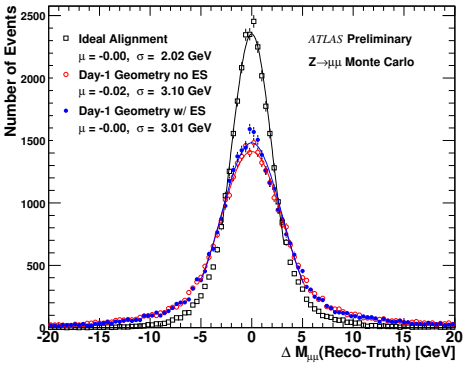

(a) $\Delta M_{\mu\mu}(\text{Reco} - \text{Truth})$ for ideal, Day-1 with ES and Day-1 without ES applied (no η restriction).

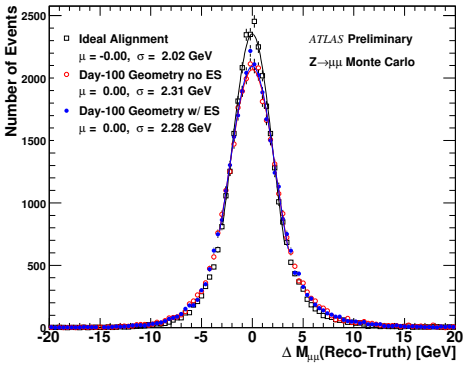

(b) $\Delta M_{\mu\mu}(\text{Reco} - \text{Truth})$ for ideal, Day-100 with ES and Day-100 without ES applied (no η restriction).

Figure 21: Impact of error scaling on the Z mass resolution when using Day-1 and Day-100 geometries in ID reconstruction.

5 Impact of Misalignments on B-Physics

5.1 Introduction and datasets

This study identifies some effects of the various types of expected ATLAS ID misalignment on B-physics observables. A detailed analysis of how performance characteristics for these observables would change under each of the misalignments was performed in order to come with a better understanding of the impact of misalignment on B-physics.

The sample consisted of 20K events with a decay $B_d^0 \to J/\psi K^{0*}$ where $J/\psi \to \mu 6\mu 4$ and $K^{0*} \to \pi^{\pm}0.5K^{\mp}0.5$ (where the trailing numbers denote the minimal p_T in GeV requested in MC generation). This sample corresponds roughly to 100 pb^{-1} . The events were simulated with CSC geometry `ATLAS-CSC-01-02-00`, using the standard `csc_evgen_trf.py`, `csc_digit_trf.py` and `csc_reco_trf.py` job transformations and all events have passed the dimuon trigger available in release 12.0.6. The definition of the geometry as well as the details about trigger were published in [3]. The events were reconstructed in Athena 14.2.20 and were analysed and passed the same requirements as in [3] (pages 1122 and 1123). After these selection cuts, the resulting sample of 8K events were used for the misalignment studies.

This B-physics chapter is organized into five sections. After this introduction, a description of the method of analysis follows in Section 5.2. The results for the two different categories of misalignments are presented and interpreted in Sections 5.3 and 5.4. Section 5.3 deals with the first category, an analysis of a local random displacement of ID modules after early ATLAS alignments. The following Section 5.4 is a study dealing with the effects of individual types of global systematic misalignments in an otherwise perfectly aligned ID. The final Section contains the conclusions and outcomes.

5.2 Method of alignment-sensitive analysis

In order to determine the impact of alignment on B-physics events, the following method was used throughout this chapter. Firstly, the misalignment was not applied at event simulation level, but instead at the reconstruction level. In this way, the same data are repeatedly reconstructed such that each time the inner detector module positions correspond to a different misalignment. The first reconstructed sample was the so-called 'ideal' alignment. This is the situation where the simulated and reconstruction alignment fully coincide. Two categories of misalignment were considered. The first category is a local random displacement of ID modules as expected after early ATLAS alignments, specifically the expected alignment after one day and after 100 days, as described in Section 2. The second category is global systematic misalignments of the detector, as described in Section 3. The following systematic misalignments: Curl, Elliptical, Telescope and Twist were analysed here (both the -Large and -Small variants in each case).

In ATLAS, the majority of B-physics events produce low-p_T particle tracks where the tracking performance is driven by the ID. Thus the factors dominating the performance of B-physics observables are the interaction of final-state particles with the material of the ID, the mapping of the solenoidal magnetic field and the alignment of the ID detector elements. All these effects combine in the J/ψ mass reconstruction as shown in Fig. 22. The reconstructed J/ψ mass was approximated by applying an unbinned maximum likelihood (UML) Gaussian fit to the reconstructed events. The maximum likelihood function is defined by:

$$L = \prod_{i=1}^{N} \frac{1}{\sigma_m \sqrt{2\pi}} e^{-\frac{(m_i - m_{J/\psi})^2}{2\sigma_m^2}} \tag{1}$$

where the index i runs over the total number of reconstructed events, and m_i is the measured mass in each event. The mass of J/ψ ($m_{J/\psi}$) and the mass resolution (σ_m) are both free parameters determined in the fit.

Figure 22 shows the J/ψ mass reconstruction using three different alignments: the ideal alignment, the Day-1 misalignment and the Day-100 misalignment. The results of the Gaussian fits in these cases are given in the figure. In this study, no mass shifts beyond the statistical precision of this test were observed due to each misalignment. The J/ψ mass resolution for an ideally aligned detector is ~ 48 MeV. An increase in the J/ψ mass resolution was observed for the misaligned cases relative to the ideal alignment case by ~ 6 % for the Day-100 and ~ 12 % for the Day-1 misalignments. Figure 23 shows the B_d^0 mass reconstruction using three different alignments: the ideal alignment, the Day-1 misalignment and the Day-100. The B_d^0 mass resolution for an ideally aligned detector is ~ 77 MeV. An increase in the B_d^0 mass resolution was observed for the misaligned cases relative to the ideal alignment case by ~ 3 % for the Day-100 and ~ 6 % for the Day-1 misalignments.

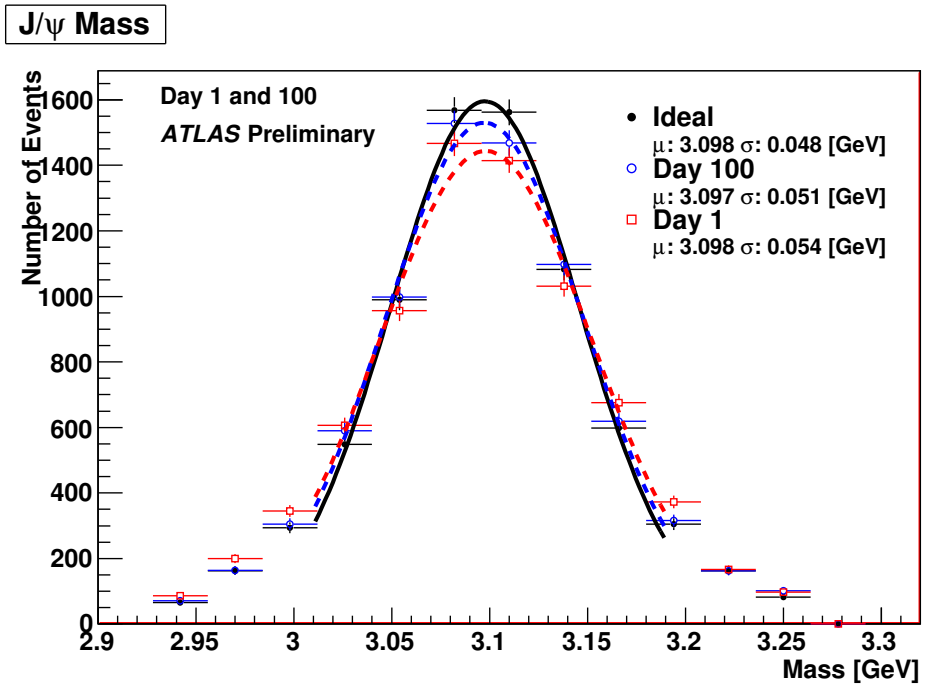

Figure 22: The reconstructed J/ψ mass fitted to a Gaussian function in three different alignment cases: ideal, Day-1 and Day-100.

In order to disentangle the alignment from other factors, an 'event-matching' technique was introduced. The 'event-matching' method takes advantage of the fact that the simulation step (modelling interactions with material of ID and trajectories of charged particles in magnetic field) is separate from the reconstruction step, where the misalignments are introduced as described above. Once the event has been simulated, the mass of J/ψ or B_d^0 meson was reconstructed several times using different alignments, giving a corresponding set of measurements, notated as: m_{ideal}, m_{twist} or m_{curl}. Any difference in these observables must arise uniquely due to differences in detector geometry. Finally, the variables Δm and $\Delta\tau$ are defined in equations (2) (3) respectively:

$$\Delta m = m_{Misaligned} - m_{Ideal} \tag{2}$$

$$\Delta\tau = \tau_{Misaligned} - \tau_{Ideal} \tag{3}$$

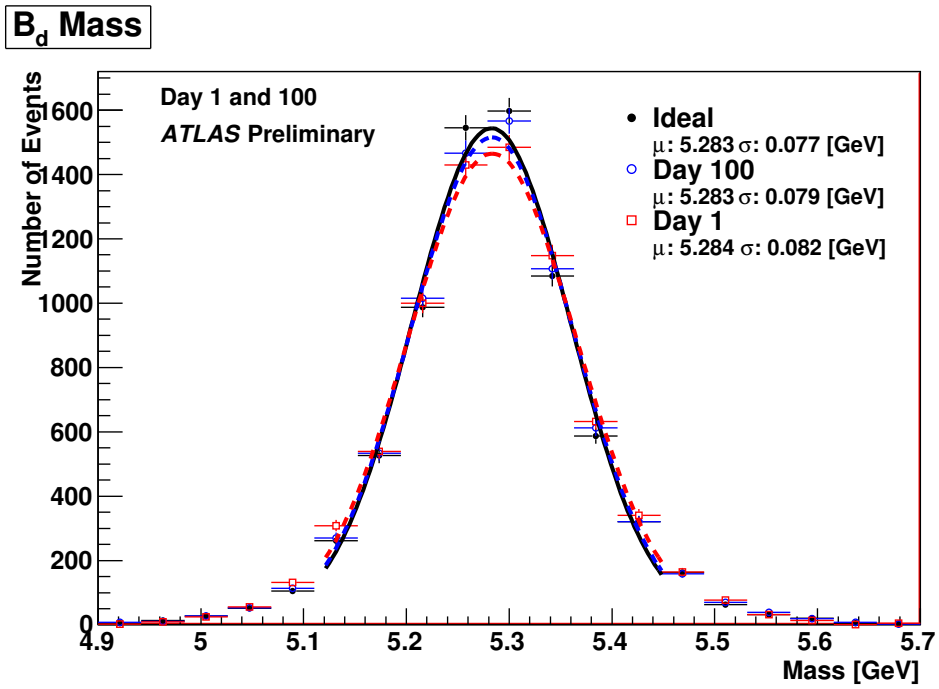

Figure 23: The reconstructed B_d^0 mass fitted to a Gaussian function in three different alignment cases: ideal, Day-1 and Day-100.

where m represents either J/ψ or B_d^0 mass, τ denotes the B_d^0 lifetime. Plotting the differences in physical variables, Δm and $\Delta\tau$ allows the direct observation of the impact of misalignment on B-physics observables.

This concept is demonstrated in Fig. 24, where a plot of $\Delta m(J/\psi)$ is shown. The dotted line shows $\Delta m(J/\psi)_1 = m(J/\psi)_{Day1} - m(J/\psi)_{Ideal}$ and the full line shows $\Delta m(J/\psi)_{100} = m(J/\psi)_{Day100} - m(J/\psi)_{Ideal}$. As expected, $\Delta m(J/\psi)_1$ is wider than $\Delta m(J/\psi)_{100}$. The analysis and interpretation of this and similar plots is given in Sections 5.3 and 5.4 that follow.

5.3 Expected B-physics Performance after 1 Day and 100 Days of Alignment

After one day, the module positions are expected to be known with precisions of order 20 μm precision for pixel and SCT modules in the barrel region. After 100 days, this uncertainty is expected to be reduced to 10 μm in the same region. This has been fully described in Section 2. Here, this section presents the impact of these misalignments on the B-physics observables: masses of B_d^0 and J/ψ , B_d^0 meson lifetime and B vertex position.

The results of a Gaussian fit to the J/ψ and B_d^0 masses have been shown in Fig. 22 and Fig. 23. A comparison of Fig. 22 to 24 highlights the value of the 'event-matching' technique. Figure 24 directly shows the amount by which the J/ψ mass resolution is degraded by the misalignments.

As described Section5.2 above, histograms were prepared for the variables $\Delta m(B_d^0)$, $\Delta m(J/\psi)$ and $\Delta\tau$ comparing the ideal alignment to Day-1 and Day-100 misalignments. The cores of these distributions were fitted by Gaussian functions. For the case of the J/ψ mass, (Fig. 24), the width of the Gaussian using Day-1 misalignments was $\sigma_1 = 23.3 \pm 0.7$ MeV. This width was reduced to $\sigma_{100} = 12.3 \pm 0.2$ MeV using the Day-100 misalignments, a factor of two that corresponds to the relative size of the misalignments in the Day-1 and Day-100 cases.

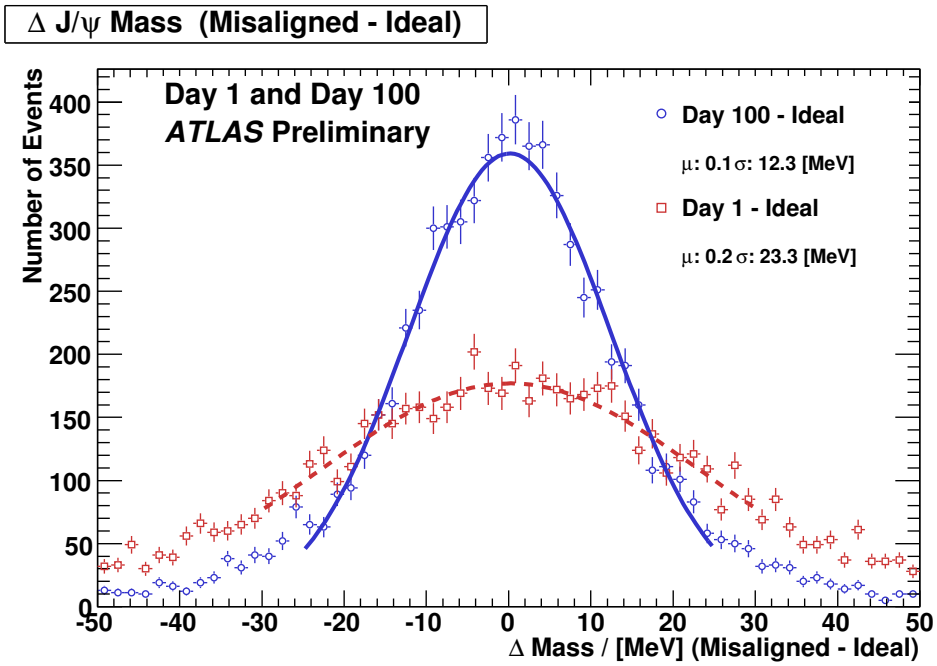

Figure 24: Comparison of J/ψ mass differences from the ideal after 100 and one day of alignments. The full line is a plot of $\Delta m_{100} = m(J/\psi_{Ideal}) - m(J/\psi_{Day100})$. The dotted line is $\Delta m_1 = m(J/\psi_{Ideal}) - m(J/\psi_{Day1})$

Figure 25 shows analogous plots to Fig. 24 for the J/ψ mass, B_d^0 mass and B_d^0 lifetime. As expected, the mass and lifetime plots show an improvement from Day-1 to Day-100 misalignments. None of the plots show a shift away from zero as expected for random misalignments.

5.4 The Impact of Global Systematic Misalignments on B-physics Observables

A weak mode is defined as a global distortion in an otherwise aligned detector that leaves the global χ^2 per degree of freedom fit unchanged. Thus, weak modes can be difficult to detect and correct by direct alignment methods (see Section 3). Even if in the early data-taking period, weak modes effects are expected to be smaller than other effects, they will have to be resolved for later high-precision measurements. A goal of this study is to identify which B-physics variables are most visibly affected, as well as identify the specific impact of each weak mode.

The four global systematic misalignments described in Section 3 have been investigated here: Curl, Twist, Elliptical and Telescope. Analogously to the expected alignment situation described in section 5.3, two sets of module positions have been considered for each misalignment: one with unrealistically large distortions and another with a either a smaller version of the same distortions (Elliptical, Telescope) or the residual distortion after alignment corrections (Curl, Twist). The previously described event-matching technique was applied to the study of the systematic misalignments and the results are shown and discussed here.

Figure 26 shows a plot of $\Delta m(J/\psi)$ for all four systematic misalignments. The dotted line shows $\Delta m(J/\psi)_{Large}$ and the full line shows $\Delta m(J/\psi)_{Residual}$. There is a marked difference in the impact of the -Large and -Small misalignments in all cases except Twist. This is consistent with the observations of Sections 3 and 4.

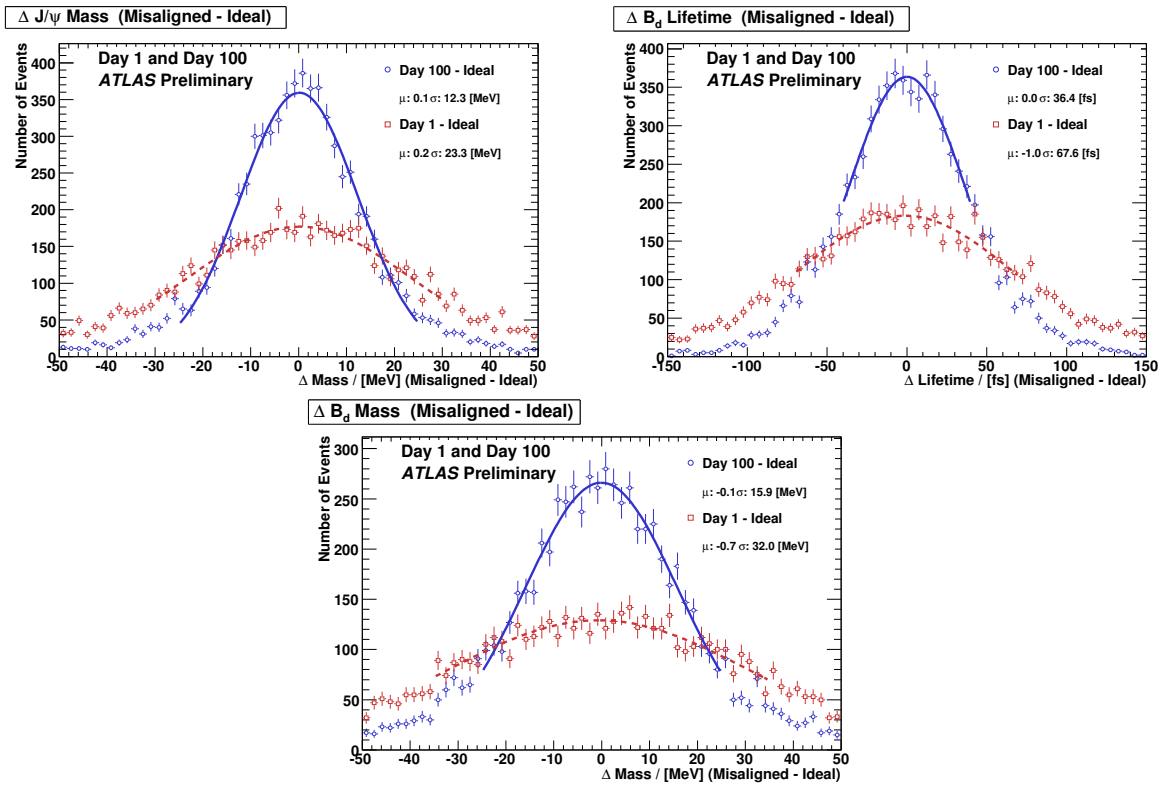

Figure 25: *top left*: J/ψ mass. *top right*: B_d^0 lifetime. *bottom*: B_d^0 mass. In all plots, the full line is a plot of $\Delta_{100} = J/\psi_{Day100} - J/\psi_{Ideal}$ and the dotted line is $\Delta_1 = J/\psi_{Day1} - J/\psi_{Ideal}$

Figure 27 shows a plot of $\Delta m(B_d^0)$ for all systematic misalignments. The dotted line shows $\Delta m(B_d^0)_{Large}$ and the full line shows $\Delta m(B_d^0)_{Residual}$. This distribution is analogous to Fig. 26. The widths of $\Delta m(B_d^0)$ distributions are larger than those in $\Delta m(J/\psi)$, since they scale as a factor of the ratio of masses $m(B_d^0)/m(J/\psi)$. For instance, comparing the effect of the Telescope-Large misalignment: $\sigma(m_{J/\psi})_{LargeTelescope} = 11.2 \pm 0.2$ MeV, where as $\sigma(m_{B_d^0})_{LargeTelescope} = 17.5 \pm 0.7$ MeV.

The largest affect on the B_d^0 lifetime is produced by the Elliptical misalignments, see the plot of $\Delta\tau(B_d^0)$ in Fig. 28. This is similar to the effects seen in the Tevatron CDF experiment [8]. Even with the Elliptical-Small misalignment, the remaining width of the Elliptical distribution, $\Delta\tau_{ellipticalResidual}$ is larger than any of the three other -Small misalignments. A dedicated study of systematic errors arising from elliptical misalignments should be a part of any B_d^0 lifetime measurements in ATLAS.

The influence of these global systematic misalignments is expected to be most dangerous in the long term. For instance, in the case of the double B_s^0 lifetime[8)] measurement (as performed at the Tevatron in [9]), the lifetime resolution for the ATLAS experiment is expected to be 85 fs. These studies indicate that the presence of global systematic misalignments could cause up to 10 fs increase in resolution width, corresponding to roughly 10%, resulting in a similar increase in measurement uncertainty. In the worse case scenario, with either a large weak mode, or some residual random misalignments similar in magnitude to the Day-1, the uncertainty in the lifetime width could increase by up to 30 fs. This would dramatically increase the statistics required to match the world's best measurement.

[8)] "Double" refers to the two components of the lifetime arising from the mixture of the two B_s^0 eigenstates.

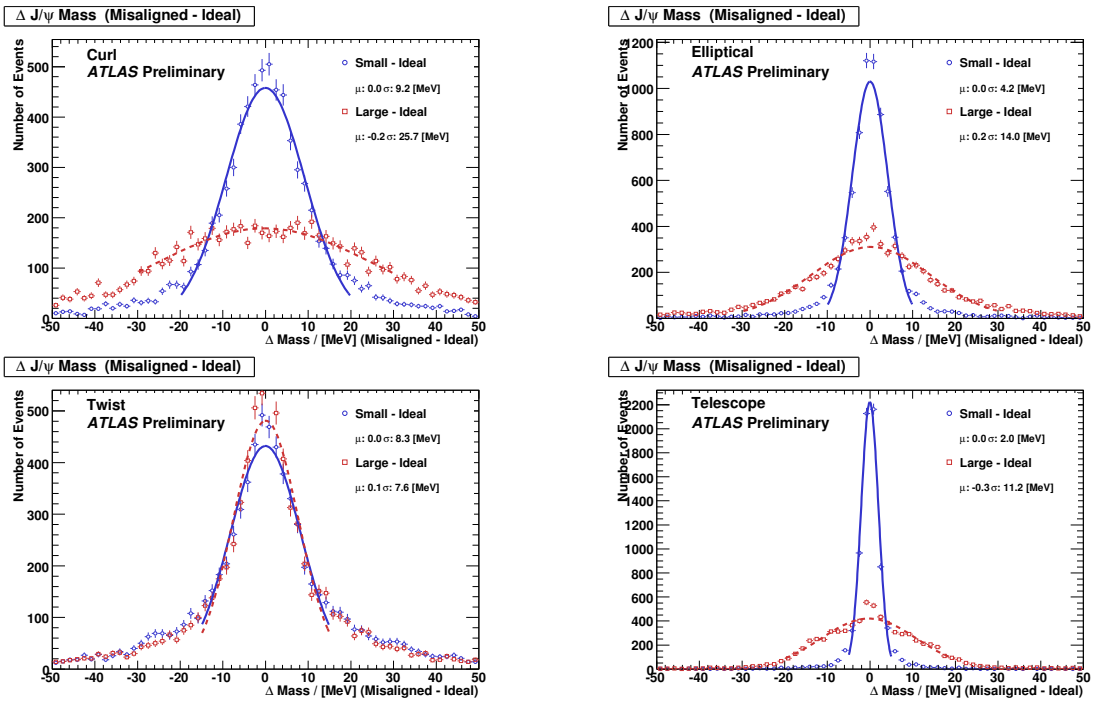

Figure 26: The influence of the four weak modes on J/ψ mass: $\Delta m(J/\psi)$

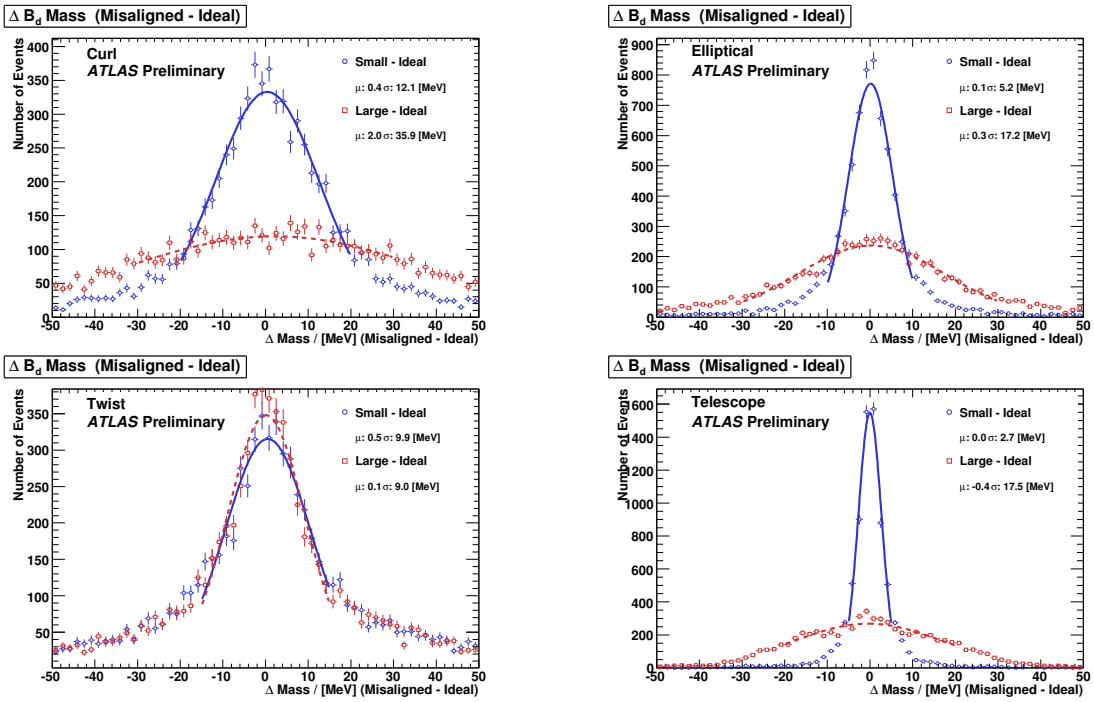

Figure 27: The influence of the four weak modes on B_d^0 mass: $\Delta m(B_d^0)$

5.5 Conclusions

Within the framework of this simulation, it was shown that for the majority of ATLAS B-physics events, the material effects of the Inner Detector are expected to overwhelm the effects of misalignment. By

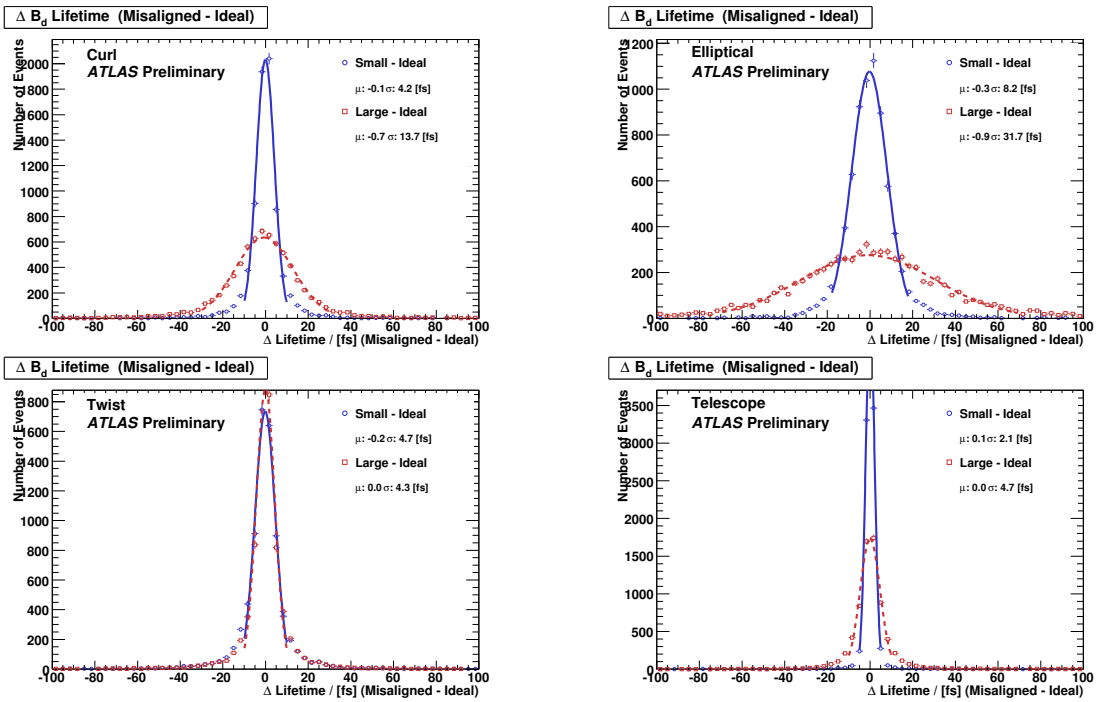

Figure 28: The influence of the four weak modes on B_d^0 lifetime, $\Delta\tau(B_d^0)$

applying an 'event-matching' method, it became possible to study separately consequences and implications of various types of misalignment. Nevertheless, for the majority of B-Physics events, the material effects from the Inner Detector are expected to overwhelm the effects of misalignment. As has been demonstrated here, the consequences for mass determinations are not likely to be large. However, more significant effects may be visible in the lifetime determinations, since this is a complicated measurement.

6 Impact of Misalignments on Tau Performance

τ-leptons can be an important probe for new physics at the LHC. Due to their short lifetime only their decay products can be reconstructed in the detector. The identification of jets from hadronic τ decays uses several calorimeter- and tracking-based quantities. Details of the τ reconstruction in ATLAS can be found in the chapter "Reconstruction and Identification of Hadronic τ Decays" of reference [3].

6.1 Introduction and datasets

This study investigates the impact of the expected misalignments referred to as Day-1 and Day-100 on the quantities used to identify hadronic τ decays. It uses Monte Carlo samples of the benchmark process $Z \rightarrow \tau\tau$ (106052). 200 K events have been re-reconstructed from ESD[9] in ATHENA 15.0.0.2 using the geometry `ATLAS-GEO-02-01-00` and sets of alignment constants based on this geometry. QCD di-jet samples (105010[10], 105011[11]) have been processed the same way to extract τ identification efficiencies as a function of jet rejection. The plots were obtained using the standard tools from the ATHENA packages `TauValidation`, `TauTrackTools` and `InDetPerformanceRTT`.

6.2 Impact on the tracking efficiency for τ decay products

Hadronic decay modes of τ leptons are divided by the number of charged pions into 1-prong and 3-prong decays. Therefore, the number of charged decay products is an important quantity to identify τ leptons. In the reconstruction of τ candidates only reconstructed tracks, which fulfil special requirements, are considered. The track selection is needed to suppress badly measured tracks or fake tracks, as well as tracks from photon conversions. Photons from the decay of neutral pions stemming from the actual τ decay may convert into e^+e^- pairs in the detector volume. Requirements like b-layer hits can efficiently reject these tracks.

The standard track selection has the following requirements:

p_T	> 1 GeV
$\lvert d_0 \rvert$	< 2 mm
$\lvert z_0 \cdot \sin(\theta) \rvert$	< 10 mm
Number of Si Hits	≥ 7

Figure 29(a) shows the efficiency for the track reconstruction using this selection. Only $\pi^{\pm}$ from hadronic τ decays (1-prong and 3-prong) are considered ($|\eta^{\mathrm{MCtruth}}| < 1.5$). No significant difference can be found for the Day-1, Day-100 or perfect alignment constants. A tighter track selection is used in the τ reconstruction to select so-called "leading" tracks in multi-track candidates:

p_T	> 1 GeV
$\lvert d_0 \rvert$	< 1 mm
$\lvert z_0 \cdot \sin(\theta) \rvert$	< 1.5 mm
Number of Si Hits	≥ 7
Number of B-layer Hits	≥ 1
Number of Pixel Hits	≥ 2

In this case the Day-1 alignment shows a drop in efficiency, which can be nearly completely recovered in the Day-100 alignment (Fig. 29(b)).

[9] `mc08.106052.PythiaZtautau.recon.ESD.e347_s462_r541`

[10] `mc08.105010.J1_pythia_jetjet.recon.ESD.e344_s465_r544`

[11] `mc08.105011.J2_pythia_jetjet.recon.ESD.e344_s465_r544`

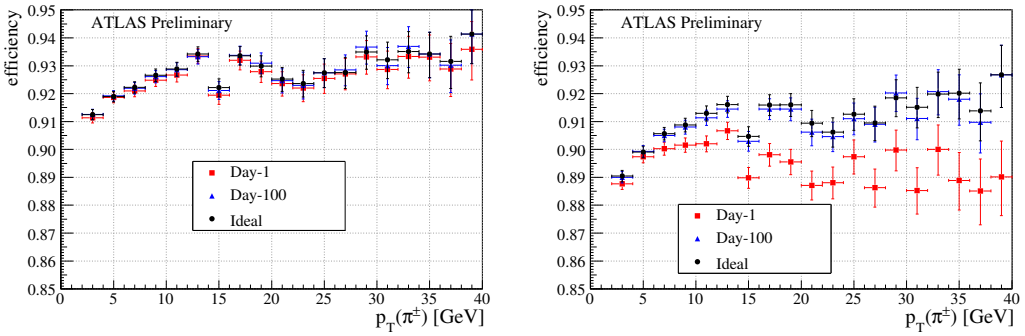

(a) Standard track selection

(b) Track selection for "leading tracks"

Figure 29: Track reconstruction efficiency for $\pi^{\pm}$ from τ decays in $Z \rightarrow \tau\tau$ events for Day-1, Day-100 and perfect alignment after applying track selection cuts as used by the τ reconstruction.

6.3 Impact on the tau identification

The results presented in the previous section are independent from the actual τ reconstruction algorithms. In this section we investigate how the effects on the track impact parameter resolution and track reconstruction efficiency propagate to the variables used by the τ reconstruction algorithms in the identification step. Figure 30 shows the impact on selected, tracking-related identification variables for track-seeded τ candidates:

1. The variance W^{τ}_{tracks}

$$W^{\tau}_{\text{tracks}} = \frac{\sum(\Delta\eta(\tau,\text{track}))^2 \cdot p_T^{\text{track}}}{\sum p_T^{\text{track}}} - \frac{(\sum \Delta\eta(\tau,\text{track}) \cdot p_T^{\text{track}})^2}{(\sum p_T^{\text{track}})^2} \tag{4}$$

2. Transverse flight path significance

3. Visible mass for 1-prong and 3-prong decays, respectively

4. Invariant mass of the track system for multi-track candidates

Only minor deviations are visible in the identification variables for the different alignment constants. Therefore no significant effects are visible in the efficiency versus rejection curves of the τ identification. Fig. 31 shows efficiency vs. rejection for 3-prong candidates from $Z \rightarrow \tau\tau$ events with visible momentum in the range 10 GeV$< p_{T\,\text{vis}}^{\text{MCtruth}} <$30 GeV. The efficiency was calculated from the $Z \rightarrow \tau\tau$ sample, whereas the jet rejection is computed from QCD di-jet samples.

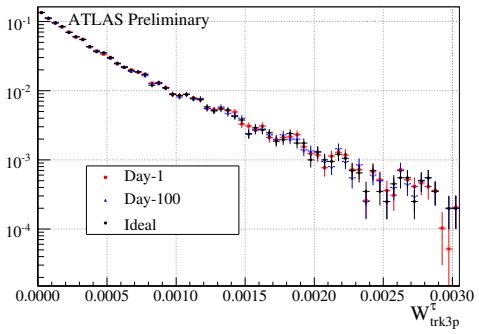

(a) The variance W^{τ}_{tracks}

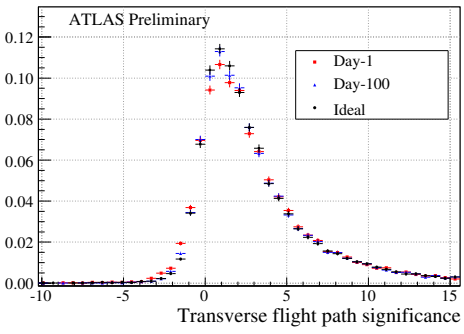

(b) Transverse flight path significance

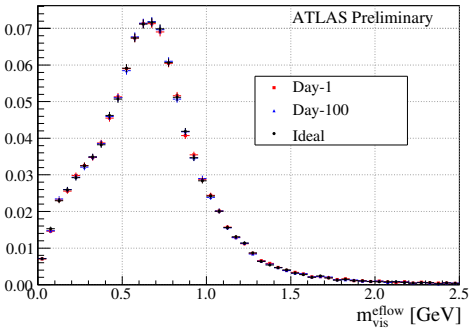

(c) Visible mass for 1-prong decays

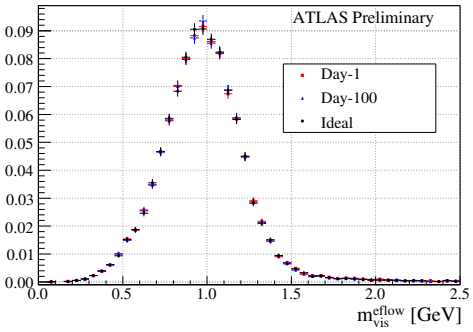

(d) Visible mass for 3-prong decays

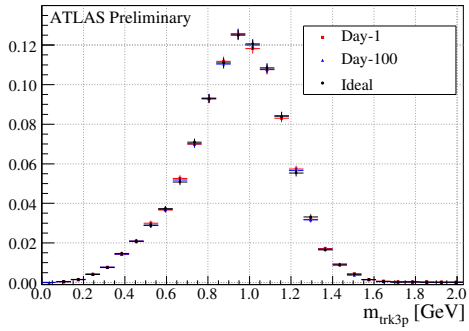

(e) Invariant mass of the track system for multi-track candidates

Figure 30: Distribution of identification variables for τ candidates with Monte Carlo truth match in $Z \to \tau\tau$ events for Day-1, Day-100 and perfect alignment.

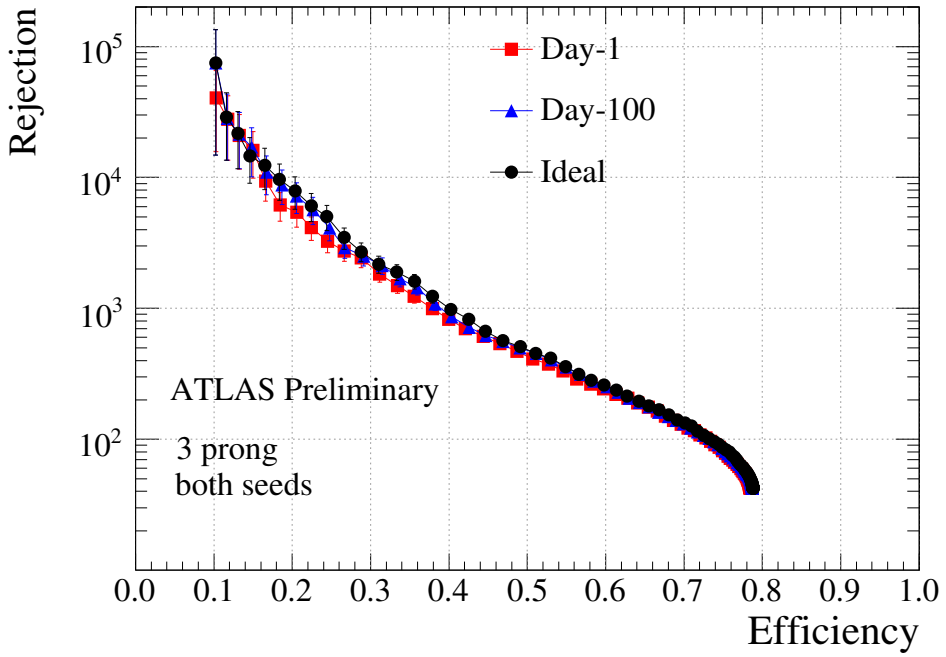

Figure 31: Tau efficiency vs rejection in the momentum range 10 GeV$< p_{T\,\mathrm{vis}}^{\mathrm{MCtruth}} <$30 GeV for $Z \rightarrow \tau\tau$ 3-prong candidates (efficiency) and QCD di-jet (rejection).

7 Impact of Misalignments on Z' Analyses

The decay of a previously undiscovered heavy vector-boson to two muons, $Z' \rightarrow \mu\mu$, could be one of the first signals of physics beyond the Standard Model (SM) at LHC. If the Z' were an exact copy of the Z boson, with mass on the order of 1 TeV, its production cross-section multiplied by branching ration $\sigma \times BR$, would be approximately 500fb. In the 1 TeV region the Standard Model (SM) background is relatively small and an integrated luminosity of the order of a few 10's of pb^{-1} is potentially enough for a discovery with 5 σ significance.

Since backgrounds are not very significant, the potential discovery relies mostly on the detector performance: the trigger and reconstruction efficiencies and muon momentum resolution. Muons with transverse momenta of the order of 500 GeV have a sagitta of the order of 200 μm and 1 mm in the Inner Detector (ID) and Muon Spectrometer (MS), respectively [12]. Therefore, any misalignment of this order of magnitude, within and between the sub-detectors, could severely impact the capability of these detectors to identify such events.

We discuss here the combined effect of ID and MS misalignments on the reconstruction of the decay $Z' \rightarrow \mu\mu$ with a boson mass of 1 TeV in the context of the Sequential Standard Model (SSM) [10]. This model is considered here as a benchmark for understanding the detector performance at the TeV scale. We have considered the following alignment scenarios for the ID and MS detectors: Ideally aligned detectors; Misalignments on the order of 500 μm (MS500) in the MS due to random shifts and rotations of the muon chambers [11]; ID with the Curl-Large geometry; ID with the Curl-Small geometry.
However, the Curl-Large and the MS500 geometries must to be considered as pessimistic cases: in fact, for the early data, we expect a misalignment of the order of 100-150 μm for the MS and something similar of Day-1 misalignment for the ID, as described in Tab. 1.

This study was performed with a dataset of about 15000 events. We run reconstruction in Athena 14.2.25.8, starting from RDO files [13] and running `csc_reco_trf.py` using a properly modified `skeleton.csc_esd.py` to load the appropriate geometry tag for MS and ID misalignments. Identical input arguments to these scripts were used as used in the r635 ATLAS official production of AODs (see Table 3).

Table 3: Input arguments used to run the reconstruction of the Z' sample.

ConditionsTag	`OFLCOND-SIM-00-00-06`
DBRelease	`DBRelease-6.5.1`
GeometryVersion	`ATLAS-GEO-02-01-00`
JobConfig	`SetJetConstants-02-000.py`
TriggerConfig	`lumi1E31_no_Bphysics_no_prescale`

For the ID with the Curl-Large and the Curl-Small geometry, we added the following lines to the skeleton file, as explained in Section 4 of [5]:

Curl-Large
```
siOverride = 'InDetSi_CSCMisaligned_RDeltaPhi_03'
```

[12] The sagitta is defined as $s(\mathrm{m}) = 0.3B(\mathrm{T})L(\mathrm{m})^2/8p_T(\mathrm{GeV})$, where for the Inner Detector $B = 2$ T and $L = 1$ m, and for the Muon Spectrometer $B = 0.4$ T and $L = 5$ m.

[13] `mc08.105601.Pythia_Zprime_mumu_SSM1000.digit.RDO.e352_s462_d154_tid045128`

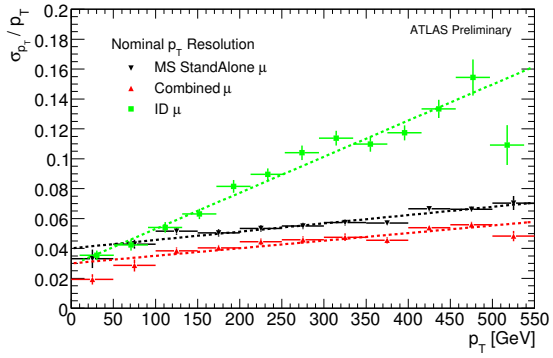

Figure 32: Relative p_T resolution as a function of the p_T for the ID (green square), MS (black downward triangle), and combined (red upward triangle) reconstructions with ideal alignment.

```
trtOverride = 'InDetTRT_CSCMisaligned_RDeltaPhi_03'
from IOVDbSvc.CondDB import conddb
include (``DetDescrCondAthenaPool/DetDescrCondAthenaPool_joboptions.py'' )
conddb.addOverride('/Indet/Align', siOverride)
conddb.addOverride('/TRT/Align', trtOverride)
```

Curl-Small

```
siOverride = 'InDetSi_CSCMisaligned_RDeltaPhi_04'
trtOverride = 'InDetTRT_CSCMisaligned_RDeltaPhi_04'
from IOVDbSvc.CondDB import conddb
include (``DetDescrCondAthenaPool/DetDescrCondAthenaPool_joboptions.py'' )
conddb.addOverride('/Indet/Align', siOverride)
conddb.addOverride('/TRT/Align', trtOverride)
```

Repeating this procedure using the default (perfect) geometry, we have obtained fully compatible results between the private and official AOD productions.

7.1 Impact on momentum resolution

The momentum resolution obtained reconstructing the Z' sample with an ideally aligned detector is shown in Fig. 32 for tracks reconstructed using the ID only, MS only, and combining the two subdetectors [14]. We will refer to muons reconstructed using the MS only as standalone, and muons reconstructed using a combination of the ID and MS as combined muons. The reconstructed invariant mass of the two muons is dominated by the momentum resolution, the contribution of the natural Z' width being of the order of few % (see Fig. 42). The resolutions are estimated by fitting with a Gaussian function the residual distribution $(p_T(\text{reco}) - p_T(\text{truth}))$ for several values of $p_T(\text{truth})$. The fit is performed in a region within $\pm$1rms around the mean value. The matching between true MC muons from Z' and reconstructed tracks is obtained by choosing the best match in $\Delta R = \sqrt{\Delta\eta^2 + \Delta\phi^2}$ and rejecting cases with $\Delta R > 400$ mrad for MS standalone tracks, and $\Delta R > 50$ mrad for ID and combined tracks. For both resolution and efficiency studies, we are considering only muons with $|\eta| < 2.5$ and $p_T > 20$ GeV.

[14] We are showing here only the resolutions obtained by the Staco and MuonBoy algorithms. With the ideal alignment, the Muid algorithms give essentially the same values.

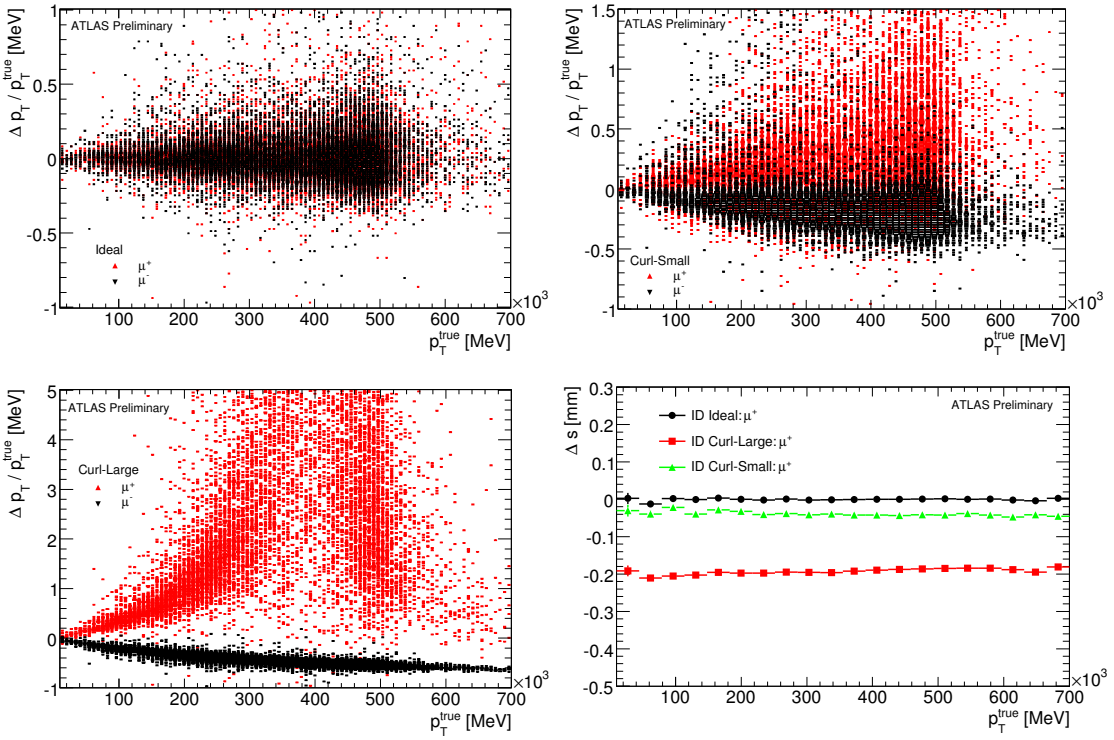

Figure 33: Relative difference between the reconstructed value of the muon p_T in the ID, minus the true muon p_T, as a function of the true p_T, in the three following cases: (Top Left) Ideal alignment; (Top Right) Curl-Small; (Bottom Left) Curl-Large. The distributions for both positive (red) and negative (black) muons are shown. Bottom right: Error on the measured sagitta for ideal (black circle), Curl-Small (green triangle), and Curl-Large (red square) alignments.

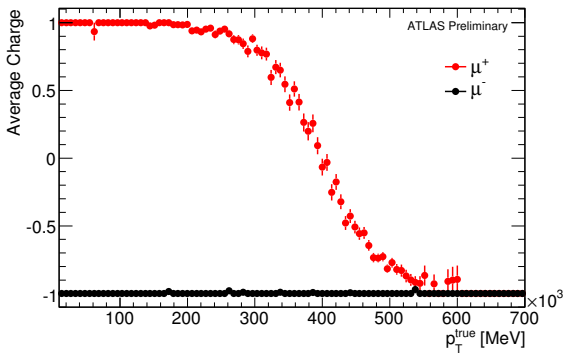

Figure 34: Average value of the muon charge identified in the ID as a function of p_T, with the Curl-Large alignment for negative (black) and positive (red) muons.

The momentum residuals for tracks reconstructed using the ID only are shown in Fig. 33. On the top-left panel, the residuals are shown for an ideally calibrated detector. On the bottom left panel of Fig. 33 we show the residuals for the Curl-Large geometry. In this case, the silicon and TRT layers are rotated along the longitudinal (Z) axis, by an amount proportional to the layer distance from the axis. The layer rotations produce a fake sagitta on the order of 200 μm, giving a positive and negative contribution for μ^- and μ^+, respectively. The negative muon momenta are decreased ($\Delta p_T = p_T(\text{reco}) - p_T(\text{truth})$), while the positive muon momenta are increased up to momenta on the order of 300 GeV, where the sagitta contribution of the track curvature and of the ID misalignment are almost equal, but with opposite sign, leading to an infinite momentum estimate. Above this momentum value, the measured charge sign is reversed (see Fig. 34), and the residuals return to lower positive values. The effect is mostly recovered in the Curl-Small case (after ID alignment), as shown on the top-right panel of Fig. 33. A residual charge asymmetry is still visible. The average residual on the measured sagitta is shown on the bottom right panel for the three alignments. The 200 μm sagitta residual obtained with the Curl-Large geometry (red squares) is reduced to about 40 μm after the calibration (green triangles) (compare with Fig. 8).

When measuring muon momenta for physics analysis purposes, we are clearly interested in the performance of the Muon Spectrometer and in the combined performance. In Fig. 35 we show the p_T resolution, as a function of the p_T, obtained by using different detector alignments and reconstruction algorithms. In each figure we compare the results obtained with a given misalignment and with the ideally aligned case. In the top panels, we shown the results obtained with the MS500 geometry, for standalone (Left) and combined (Right) tracks. When a misalignment on the order of 500 μm is introduced, the relative resolution for standalone muons, MuonBoy and MuidSA, worsens to values of about 50% at 500 GeV, as expected for a sagitta on the order of 1 mm. When the MS tracks are combined with (aligned-) ID tracks, by the algorithms Staco and MuidCB, about half of the effect is recovered. In the middle plots, we show the results obtained for combined tracks with the ID Curl-Large geometry. The standalone resolution is clearly unchanged, and is not shown here. The resolutions for combined positive and negative tracks show a different behaviour. For positive muons the 200 μm systematic shift reduces the sagitta, increasing the relative error on the momentum; for negative muons it increases the sagitta, reducing its relative error. In the bottom plots, we show the resolutions for combined tracks of positive muons with the MS500+Curl-Large (Left) and MS500+Curl-Small (Right) misalignments. Comparing the two bottom plots to the top right we can see that a substantial additional degradation of the combined muon p_T resolution is only seen when using the more extreme Curl-Large ID deformation. However, it must be stressed that with the Curl geometries, large tails appear in the residual distributions, as can be

inferred from Fig. 34. In this case, the Gaussian approximation used to fit the distributions is no longer valid, and the results obtained have to be taken with care.

In Fig. 36, we show the distribution of the difference of measured and expected transverse momentum, $1/p_T(\text{reco}) - 1/p_T(\text{truth})$, for the same detector alignments and reconstruction algorithms as in Fig. 35. In the high p_T region, $\sigma(1/p_T)$ is approximately a constant, and systematic errors on the sagitta lead to a shift in the distributions. Therefore, essentially the same considerations done for Fig. 35 can be derived from these pictures. For each distribution, we also show the value of the mean and standard deviation from a Gaussian fit, obtained in a region within ± 1 rms around the peak. From the middle plots, we can also see the large tails of the inverse-momentum residuals that appear when reconstructing with the Curl-Large geometry.

7.2 Impact on track efficiency

While the resolution must be optimized for a good signal to background ratio, in the search for new physics channels it is essential to keep the selection efficiency as high as possible. In fact the luminosity required for the discovery is inversely proportional to the selection efficiency. In Fig. 37 we show the reconstruction efficiency for tracks reconstructed in the ID only, and for MS standalone reconstruction with the MuonBoy and MuidSA algorithms, with different detector alignments. Reconstruction efficiencies are obtained by counting the fraction of true muons identified as coming from a Z' that match to a reconstructed track, using the same matching criteria as was described in the previous section. We estimated the inefficiency due to the cone size definition to be at most few %. One can see from Fig. 37 that the standalone reconstruction is essentially insensitive to even the maximal misalignments considered in this work.

The situation changes when the efficiency for combined muon reconstruction is considered. In Fig. 38, we show the reconstruction efficiency for combined muons using both the Staco and MuidCB algorithms, again for several different alignments of the detector.

One can see that for all of the misaligned cases, with the exception of the Curl-Small, that the efficiency drops to lower values at high p_T compared with the perfect alignment case. Here, we also observe, for the first time, a very different behaviour for the two reconstruction algorithms Staco and MuidCB. The drop in efficiency between the two is very similar when the MS500 geometry is used (red squares). However, when the Curl-Large geometry is used (green upward-triangle), the Staco reconstruction efficiency is insensitive to the misalignments in the ID (up to few %), while the efficency for the MuidCB algorithm drops down to 40%. Since the standalone efficiencies are unchanged when the misalignments are introduced, this effect is presumably due to the reduced probability of combining the ID and MS tracks. In order to verify this hypothesis, we loosened the χ^2 cut used in the track reconstruction algorithm for matching ID and MS tracks [15], by changing it from the default value (30) to an arbitrary large value (10,000). In Fig. 39, we see that the efficiency drop observed with the Curl-Large geometry (green triangles) is recovered when using this looser matching criteria (red squares). Further studies are needed to understand the impact of a looser matching criteria on the fake rates. However, the inclusion in the calculation of the χ^2 of a term that takes into account the detector misalignment should help in increasing the algorithm robustness.

In the following, only the default reconstruction has been considered. Since the Event Filter trigger level (EF) uses MuidCB as tracking algorithm, the observed inefficiency reflects on the trigger performance, as discussed in the next section.

[15] MuidMatchMaker.MatchChiSquaredCut = 10000

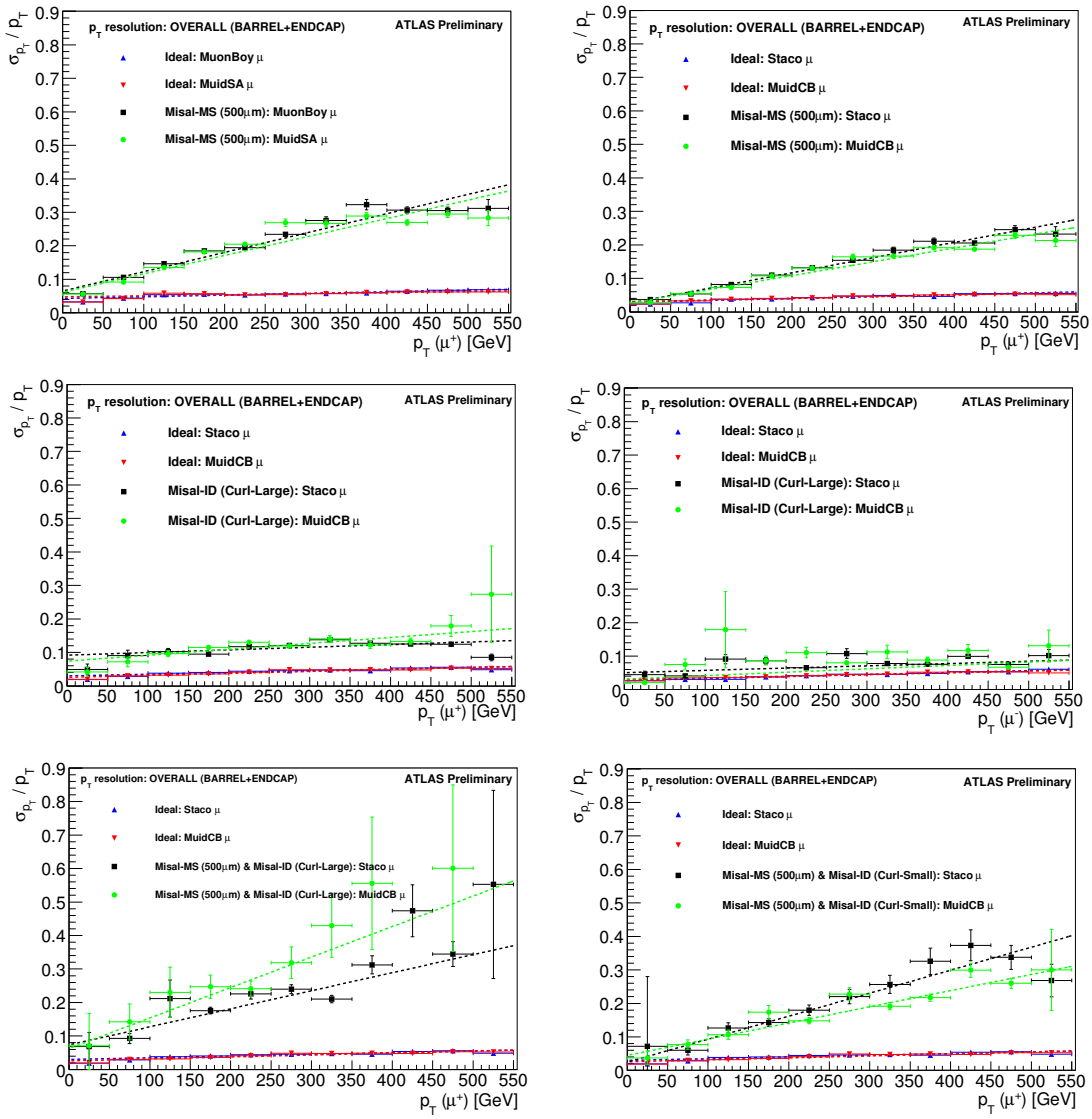

Figure 35: Comparison of relative p_T resolution as a function of the true p_T, obtained with misaligned and aligned geometries. Results for MuonBoy or Staco are represented with an upward blue triangle for ideal alignment and with a black square for misaligned geometries. Results for MuidSA or MuidCB are represented with a downward red triangle for ideal alignment and with a green circle for misaligned geometries. Top: MS500 misalignment, for standalone (Right) and combined (Left) tracks. Middle: Combined reconstruction with Curl-Large for positive (Left) and negative (Right) muons. Bottom: Combined reconstruction for positive muons with MS500+Curl-Large (Left) and MS500+Curl-Small (Right).

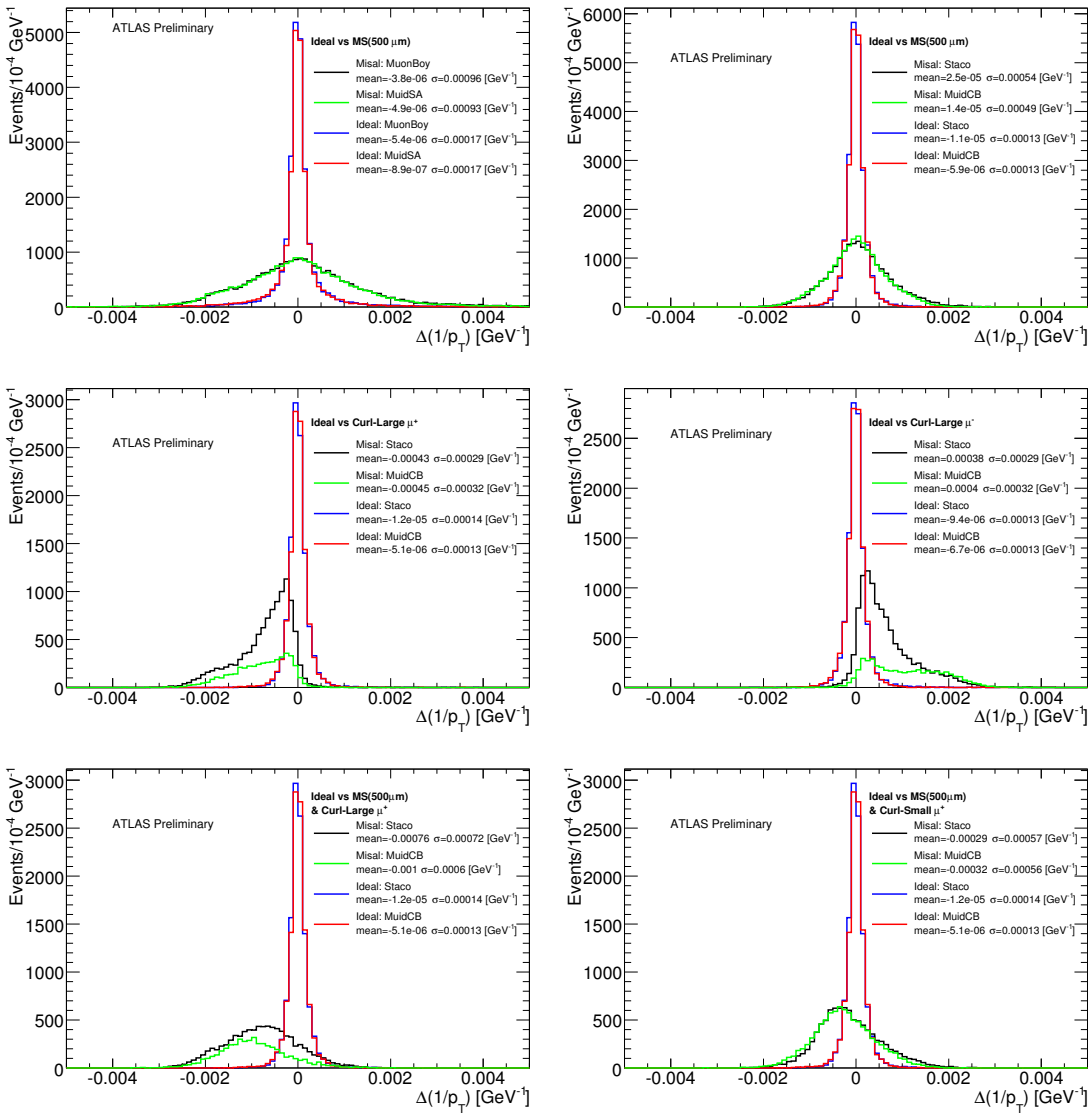

Figure 36: Comparison of $1/p_T(\text{reco}) - 1/p_T(\text{truth})$, obtained with misaligned and aligned geometries. Results for MuonBoy or Staco are represented with a blue line for ideal alignment and with a black line for misaligned geometries. Results for MuidSA or MuidCB are represented with a red line for ideal alignment and with a green line for misaligned geometries. Top: MS500 misalignment, for standalone (Right) and combined (Left) tracks. Middle: Combined reconstruction with Curl-Large for positive (Left) and negative (Right) muons. Bottom: Combined reconstruction for positive muons with MS500+Curl-Large (Left) and MS500+Curl-Small (Right). For each distribution we show also the mean and standard deviation from a Gaussian fit in a region within ± 1 rms around the peak.

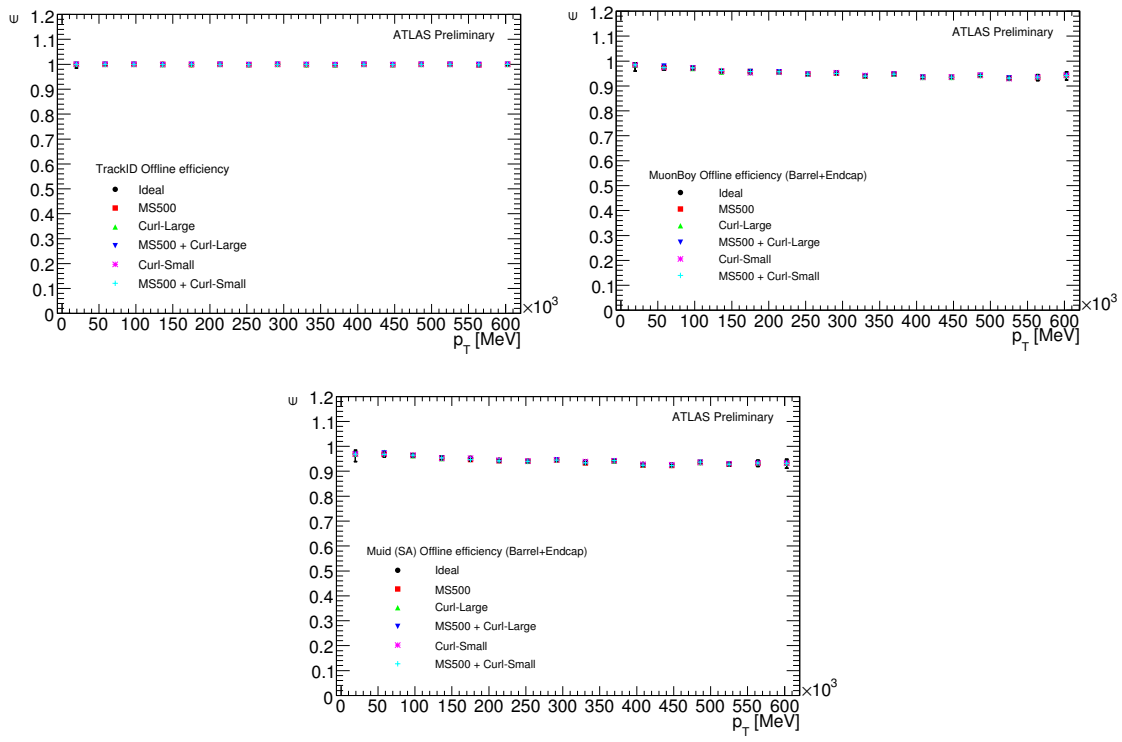

Figure 37: Track reconstruction efficiency as a function of the true p_T, for ID tracks (Top left), MuonBoy (Top right), and MuidSA (Bottom). Values are shown for several alignment of the detector: Aligned (black circle); MS500 (red square); Curl-Large (green upward-triangle); MS500+Curl-Large (blue downward-triangle); Curl-Small (pink asterisk); MS500+Curl-Small (light blue cross).

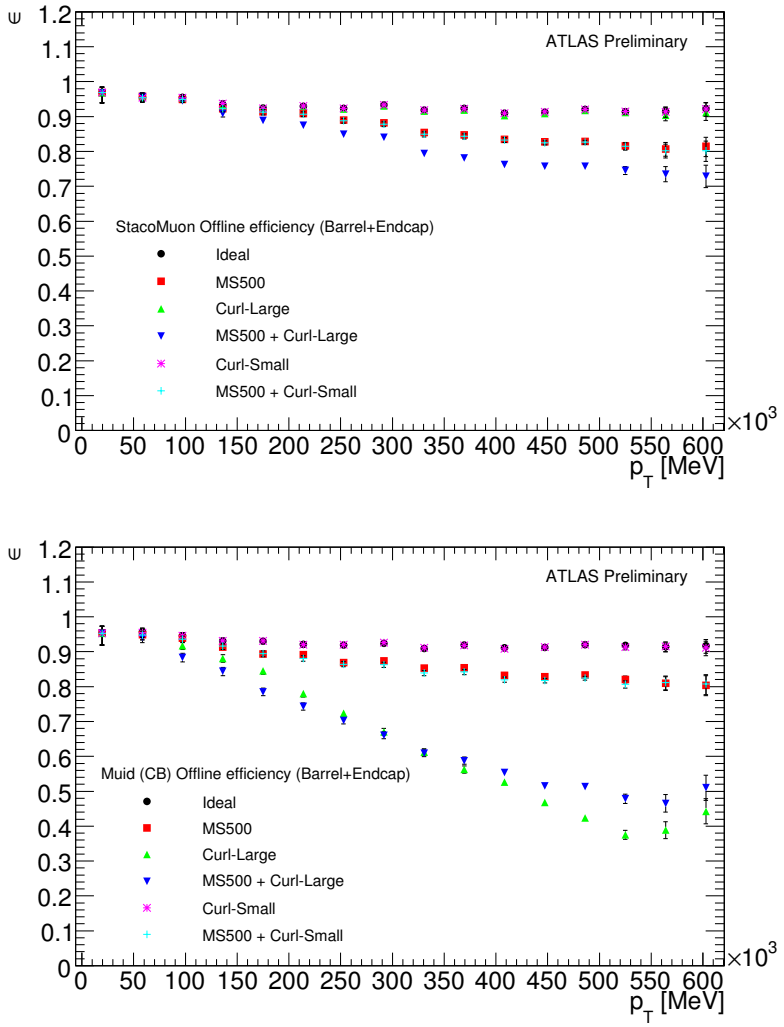

Figure 38: Track reconstruction efficiency as a function of the true p_T, for combined tracks: Staco (Top); MuidCB (Bottom). Values are shown for several alignment of the detector: Aligned (black circle); MS500 (red square); Curl-Large (green upward-triangle); MS500+Curl-Large (blue downward-triangle); Curl-Small (pink asterisk); MS500+Curl-Small (light blue cross).

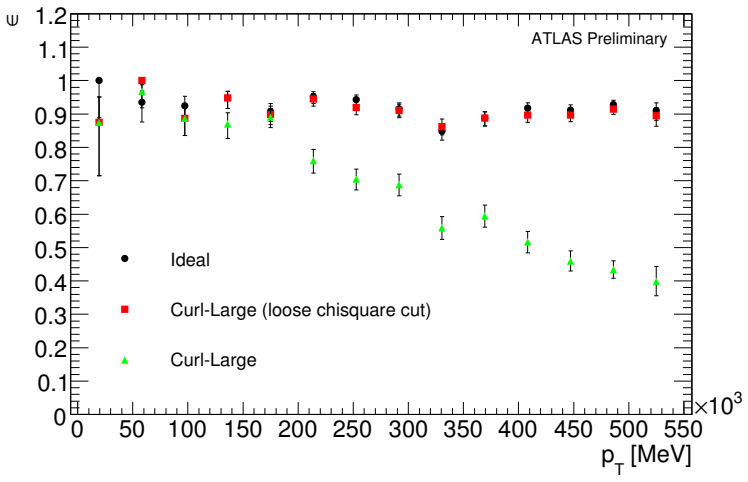

Figure 39: Track reconstruction efficiency as a function of the true p_T, for MuidCB combined tracks: for aligned detector (black dots); for Curl-Large misalignment (green triangles); for Curl-Large misalignment but loosening the χ^2 cut in reconstruction (red squares).

7.3 Impact on trigger efficiency

In Fig. 40, we show the relative efficiency for the three levels of the trigger, the hardware (L1), and the software levels (L2 and EF), when requiring at least one combined muon with $p_T > 20$ GeV ($\mu 20$ chain). In defining this efficiency the matching between true muons and L1 ROIs or L2 and EF trigger features has been done in a way similar as done for the tracks in the previous sections. The size of the matching cone, ΔR, has been chosen equal to 300, 100, and 50 mrad for L1, L2, and EF, respectively. Inefficiency losses due to the cone size are estimated to be less than few %.

We can immediately observe that while the L1 and L2 levels are insensitive to the misalignments, even large ones, the EF level reproduces the same behaviour observed in Fig. 38 (Bottom) for the MuidCB algorithm. It has to be stressed again, that only this last algorithm is used for reconstructing and combining MS tracks at trigger level. Therefore, even if the offline reconstruction is done with the Staco algorithm, a large loss of events would be expected. For completeness, we also show the η behaviour of the efficiency for the EF level in Fig. 41.

Finally, two more comments are needed. First, most of the effects observed with the Curl-Large geometry have to be considered as pessimistic. The Curl-Small geometry is considered a more realistic misalignment scenario since this has been corrected by the ID alignment procedure. In the Curl-Small case, most of the efficiency loss is recovered. Second, it is foreseen to have a MS-standalone trigger, at least for the first data, in order to avoid any effect related to the inter-calibration of the two detectors.

7.4 Impact on selection

After a general discussion on the detector performance in the high-p_T region in presence of misalignments, we discuss here the impact on the $Z' \rightarrow \mu\mu$ channel, in particular the effect on the invariant mass reconstruction and on the selection efficiency. Unfortunately, no final result of the impact on the discovery potential can be given here since this work is not completed yet.

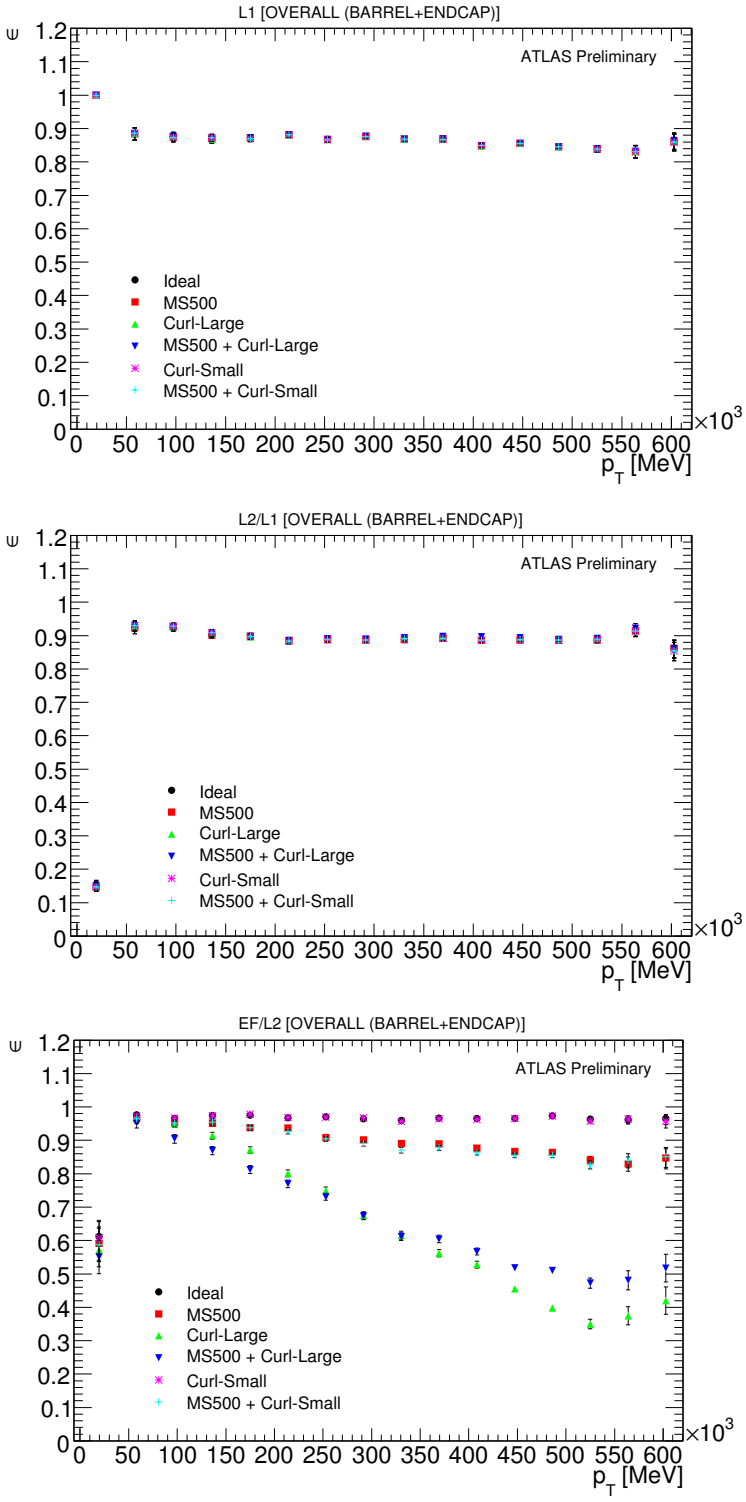

Figure 40: Efficiency for the three trigger levels, in the $\mu 20$ chain, as a function of the true p_T: (Top) L1; (Middle) L2/L1; (Bottom) EF/L2. Values are shown for several alignment of the detector: Aligned (black circle); MS500 (red square); Curl-Large (green upward-triangle); MS500+Curl-Large (blue downward-triangle); Curl-Small (pink asterisk); MS500+Curl-Small (light blue cross).

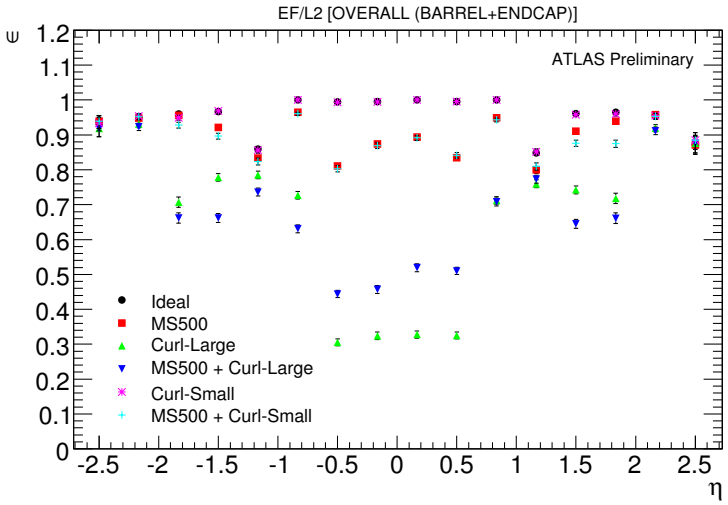

Figure 41: Efficiency for the EF trigger level (chain $\mu 20$), with respect to level 2, as a function of η. Values are shown for several alignment of the detector: Aligned (black circle); MS500 (red square); Curl-Large (green upward-triangle); MS500+Curl-Large (blue downward-triangle); Curl-Small (pink asterisk); MS500+Curl-Small (light blue cross).

Z' events are selected by requiring two reconstructed muon tracks, standalone or combined, with opposite charge, $|\eta| < 2.5$, and $p_T > 20$ GeV. We keep all events with invariant mass within 500 and 1500 GeV and satisfying the $\mu 20$ trigger chain.

In Fig. 42, we show the reconstructed invariant mass of the two muons with different detector misalignments, starting from the best case (ideal alignment, top left panel), to the worst case (MS500+Curl-Large). The width of the Z' peak is dominated by the momentum resolution, even in the perfect alignment case. Beside the boson peak, we observe the contribution of the continuum Drell-Yan process. With an aligned detector, the peak is more pronounced when using combined muons (red and blue histograms). With the Curl-Small geometry (top right panel), this difference is not so evident anymore. However, the signal peak is still clearly visible. When the Curl-Large geometry is used (middle left panel), the signal is only well visible with standalone muon tracks (black and green histograms). The Staco algorithm (red histogram) is less sensitive to the misalignment than the MuidCB (blue histogram). In the middle right panel we show the effect of the MS500 geometry. The resolution is worsened for all four reconstruction algorithms. It would be interesting to study the invariant mass resolution obtained using only ID tracks, tagged as muons by the MS. In the bottom plots we show the effect of the combined geometries MS500+Curl-Small and MS500+Curl-Large. In the last case, the invariant mass distribution is so washed out that it becomes hard to distinguish from the expected pure Drell-Yan distribution [16].

The selection efficiency after each cut is shown in Tabs. 4 and 5, for all the alignments considered. The total efficiency goes from about 70% with the ideal alignment and using combined tracks, down to about 27% with the Curl-Large geometry for combined track reconstructed with the MuidCB algorithm. The losses due to trigger failure are clearly not recovered when using the Staco or standalone algorithms. The large impact of the extreme Curl-Large deformation is considerably mitigated when the more realistic Curl-Small deformation is used. Once the misalignments in the ID are reduced to the Curl-Small

[16] In the sample we have used, the Drell-Yan contribution is simulated only starting from an invariant mass of 500 GeV. So in these plots we are probably missing the contribution of events coming from lower values of the invariant mass.

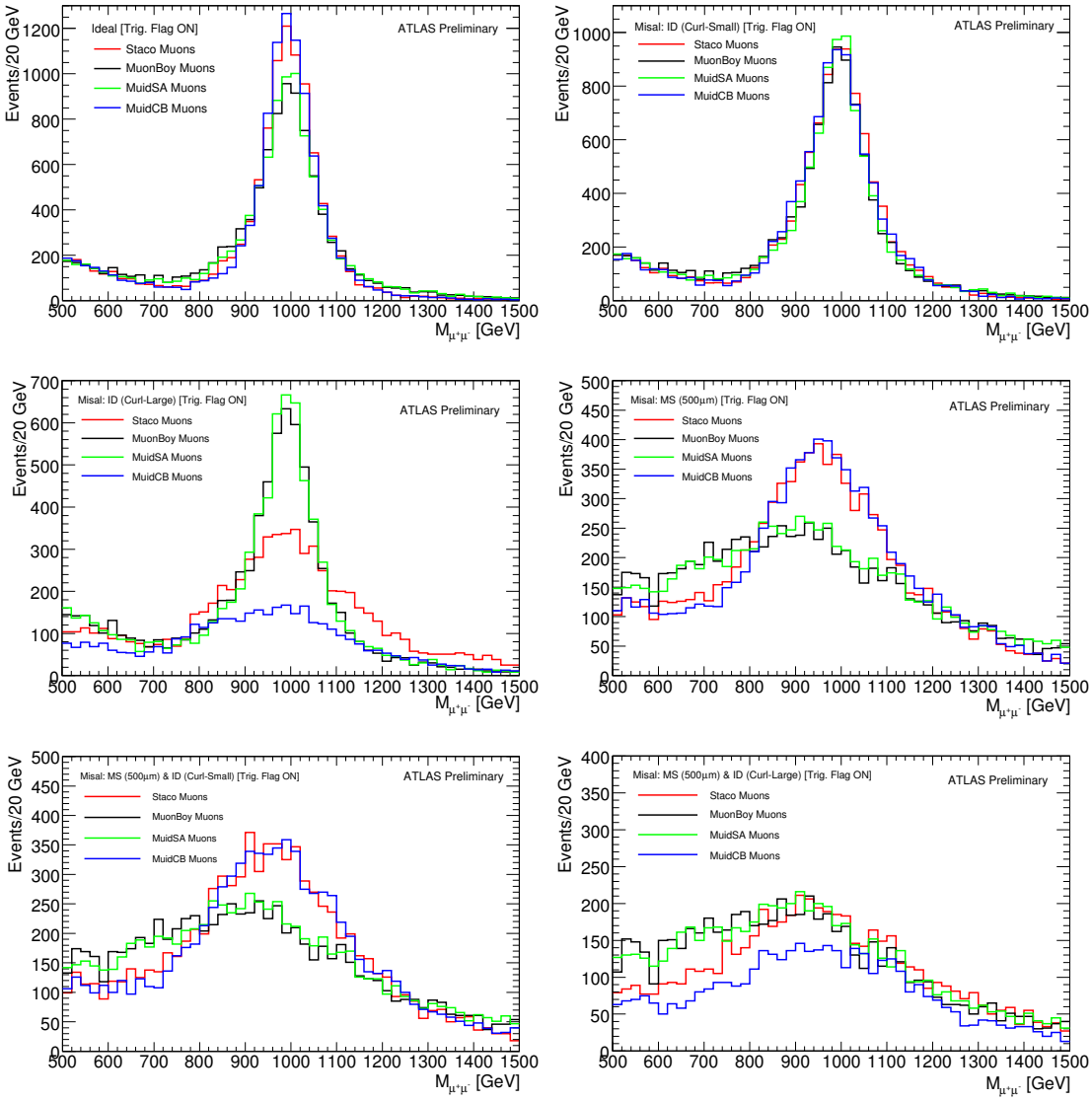

Figure 42: Reconstructed invariant mass of the two muons for the process $pp \to \gamma^*/Z' \to \mu\mu$. Starting from the top left picture, the events are reconstructed with the following detector alignment: Ideal alignment; Curl-Small; Curl-Large; MS500; MS500+Curl-Small; MS500+Curl-Large. Different track reconstructions are shown with different colors: Staco (Red); MuonBoy (black); MuidSA (green); MuidCB (blue).

Table 4: Selection efficiencies (%) after each cut, for tracks reconstructed with standalone or combined algorithm, with several detector alignments.

Ideal alignment

Reconstruction/Cut	2 tracks	p_T-cut	charge	$M_{\mu\mu} - cut$	trigger
MuonBoy	83.3 ± 0.3	78.7 ± 0.3	76.4 ± 0.3	71.2 ± 0.4	68.1 ± 0.4
Staco	76.4 ± 0.3	75.3 ± 0.4	75.3 ± 0.4	72.8 ± 0.4	69.6 ± 0.4
MuidSA	82.6 ± 0.3	77.1 ± 0.3	75.1 ± 0.4	70.4 ± 0.4	67.5 ± 0.4
MuidCB	76.2 ± 0.3	75.1 ± 0.4	75.0 ± 0.4	72.5 ± 0.4	69.7 ± 0.4

MS500

Reconstruction/Cut	2 tracks	p_T-cut	charge	$M_{\mu\mu} - cut$	trigger
MuonBoy	83.3 ± 0.3	78.6 ± 0.3	70.7 ± 0.4	55.5 ± 0.4	52.1 ± 0.4
Staco	66.5 ± 0.4	65.3 ± 0.4	65.2 ± 0.4	60.7 ± 0.4	56.7 ± 0.4
MuidSA	82.3 ± 0.3	76.9 ± 0.3	69.5 ± 0.4	55.7 ± 0.4	52.8 ± 0.4
MuidCB	66.1 ± 0.4	64.7 ± 0.4	64.6 ± 0.4	59.4 ± 0.4	56.9 ± 0.4

Curl-Small

Reconstruction/Cut	2 tracks	p_T-cut	charge	$M_{\mu\mu} - cut$	trigger
MuonBoy	83.3 ± 0.3	78.7 ± 0.3	76.4 ± 0.3	71.2 ± 0.4	68.0 ± 0.4
Staco	76.5 ± 0.3	75.4 ± 0.4	75.3 ± 0.4	72.6 ± 0.4	69.3 ± 0.4
MuidSA	82.7 ± 0.3	77.2 ± 0.3	75.2 ± 0.4	70.4 ± 0.4	67.5 ± 0.4
MuidCB	76.2 ± 0.4	75.0 ± 0.4	74.9 ± 0.4	72.1 ± 0.4	69.2 ± 0.4

Curl-Large

Reconstruction/Cut	2 tracks	p_T-cut	charge	$M_{\mu\mu} - cut$	trigger
MuonBoy	83.3 ± 0.3	78.7 ± 0.3	76.4 ± 0.4	71.2 ± 0.4	49.9 ± 0.4
Staco	75.9 ± 0.4	74.8 ± 0.4	74.1 ± 0.4	67.2 ± 0.4	47.5 ± 0.4
MuidSA	82.6 ± 0.3	77.2 ± 0.3	75.2 ± 0.4	70.4 ± 0.4	50.0 ± 0.4
MuidCB	32.2 ± 0.4	30.8 ± 0.4	30.6 ± 0.4	28.2 ± 0.4	26.6 ± 0.4

MS500+Curl-Small

Reconstruction/Cut	2 tracks	p_T-cut	charge	$M_{\mu\mu} - cut$	trigger
MuonBoy	83.3 ± 0.3	78.6 ± 0.3	70.6 ± 0.4	55.6 ± 0.4	51.9 ± 0.4
Staco	66.2 ± 0.4	65.0 ± 0.4	64.8 ± 0.4	60.1 ± 0.4	56.0 ± 0.4
MuidSA	82.4 ± 0.3	77.0 ± 0.3	69.6 ± 0.4	55.8 ± 0.4	52.5 ± 0.4
MuidCB	64.6 ± 0.4	63.3 ± 0.4	63.1 ± 0.4	58.0 ± 0.4	55.5 ± 0.4

Table 5: Selection efficiencies (%) after each cut, for tracks reconstructed with standalone or combined algorithm. Continues from Tab. 4.

MS500+Curl-Large

Reconstruction/Cut	2 tracks	p_T-cut	charge	$M_{\mu\mu} - cut$	trigger
MuonBoy	83.3 ± 0.3	78.6 ± 0.3	70.7 ± 0.4	55.6 ± 0.4	41.4 ± 0.4
Staco	58.3 ± 0.4	57.0 ± 0.4	55.8 ± 0.4	48.6 ± 0.4	38.3 ± 0.4
MuidSA	82.3 ± 0.3	76.9 ± 0.3	69.6 ± 0.4	55.8 ± 0.4	42.1 ± 0.4
MuidCB	34.6 ± 0.4	33.0 ± 0.4	32.4 ± 0.4	29.1 ± 0.4	27.7 ± 0.4

level, the MS random misalignment dominates, as can be seen in the column $M_{\mu\mu} - cut$ of the MS500 sub-table in Tab. 4.

8 Summary and Conclusion

The impact of random and global systematic misalignments of the Inner Detector and random misalignments of the Muon Spectrometer on selected physics processes has been investigated. Random ID misalignments corresponding to the expected alignment precision on the first day (Day-1) and the hundredth day (Day-100) of collisions data taking have been used. Several types of global systematic ID misalignments have been produced via simple parameterisations of individual module shifts, and their compatibility with weak mode misalignments has been demonstrated.

The Day-1 and Day-100 random ID misalignments have been shown to produce a degradation in the $Z \rightarrow \mu\mu$ mass resolution when constructing the mass from the muon tracks in the ID. Even when using the smaller Day-100 misalignments, the Z mass resolution is degraded by 13% relative to the ideal alignment case. However, studies on a $B_d^0 \rightarrow J/\psi K^{0*}$ sample indicate that the impact of these random misalignments on J/ψ and B_d^0 mass reconstruction is not significant. Using the larger Day-1 random misalignments the J/ψ mass resolution is increased by only $\sim 10\%$ (~ 23 MeV added in quadrature to the ideal alignment resolution of ~ 48 MeV), with a similar impact observed in the B_d^0 mass resolution (~ 32 MeV added in quadrature to the ideal alignment resolution of ~ 77 MeV). The impact of the random Day-1 and Day-100 ID misalignments on Tau identification performance has also been studied, and no significant impact of the misalignments was observed.

The Curl global systematic ID misalignment has been observed to produce a charge dependent curvature bias on ID reconstructed tracks, which translates into a bias on the reconstructed track momenta. Two different magnitudes of Curl misalignment were investigated, labelled Curl-Large and Curl-Small, which produce p_T-biases of $\sim 14\%$ and $\sim 2\%$ respectively. The Curl-Small misalignment was produced by running the Global χ^2alignment algorithm on a Curl-Large misaligned geometry, and thus this demonstrates the success of this algorithm in correcting the misalignment to some extent. With greater collision data statistics and the use of additional event types (cosmic rays, beam gas, beam halo) it is expected that the Curl misalignment would be further reduced.

The p_T-biases of the Curl ID misalignments result in a significant degradation of the $Z \rightarrow \mu\mu$ mass resolution, by $\sim 30\%$ and $\sim 20\%$ in the Curl-Large and Curl-Small cases respectively. However, the impact of the misalignments is much less significant for J/ψ and B_d^0 reconstruction. The Curl-Large misalignment increases the J/ψ mass resolution by only $\sim 14\%$ (~ 26 MeV added in quadrature to the ideal alignment resolution of ~ 48 MeV), with a similar impact observed in the B_d^0 mass resolution. The Curl-Small misalignment has a greatly reduced effect on these observables.

Overall these results show that, due to the intrinsically low p_T of the decay products, the J/ψ and B_d^0 mass resolutions are dominated by material interactions rather than ID misalignments. Misalignments have a more significant impact in Z mass reconstruction, where the p_T of the decay products is typically much larger.

The impact of random MS misalignments and of the Curl-Small and Curl-Large ID misalignment on the reconstruction of muons using the ID only, the MS standalone and ID+MS combined algorithms was investigated. As one might expect the random MS misalignments used, which are large compared with the desired MS alignment precision of 30 μm, were found to have a substantial impact on the standalone muon p_T resolution, an affect that can be mitigated by using combined algorithms. However, they also impact the combined muon reconstruction efficiency at high-p_T (above 400 GeV). The Curl-Large deformation was observed to have a large impact on combined muon reconstruction in this high p_T region when using the Muid algorithm (and hence the EF trigger efficiency). This affect is thought to be due to the misalignments introduced between the ID and MS introduced by this deformation, and thus is something which could be substantially reduced by performing a relative MS-ID alignment (which has

not been done here). In addition, the affect virtually disappears when using the less extreme and more "realistic" Curl-Small misalignment.

References

[1] The ATLAS collaboration, "Inner Detector: Technical Design Report", CERN/LHCC/97-016/017 (2009).

[2] The ATLAS collaboration, "The ATLAS Experiment at the CERN Large Hadron Collider", JINST 3 S08003, (2008).

[3] Aad, G. et al. , ATLAS collaboration, "Expected Performance of the ATLAS Experiment : Detector, Trigger and Physics", CERN-OPEN-2008-020, (2009)

[4] D. N. Brown, A. V. Gritsan, Z. J. Guo and D. Roberts, "Local Alignment of the BABAR Silicon Vertex Tracking Detector", arXiv:0809.3823 [physics.ins-det].

[5] Alison, J; Cooper, B; Goettfert, T, "Production of Systematically Misaligned Geometries for the ATLAS Inner Detector", ATL-COM-INDET-2009-003, (2009).

[6] P. Bruckman, A. Hicheur, S. Haywood, "Global χ^2 approach to the Alignment of the ATLAS Silicon Tracking Detectors", ATL-INDET-PUB-2005-002 (2005).

[7] J. Alison et al. , "Alignment of the Inner Detector using misaligned CSC data", ATL-COM-INDET-2008-014 (2008).

[8] Acosta, D. et al. , "Measurement of b hadron masses in exclusive J/ψ decays with the CDF detector", Phys. Rev. Lett. 96: 202001, FERMILAB-PUB-05-316-E (2006)

[9] T. Aaltonen, et al. , "Measurement of Lifetime and Decay-Width Difference in $B_s^0 \to J/\psi\phi$ Decays", Phys. Rev. Lett. 100: 121803, FERMILAB-PUB-07-655-E (2008)

[10] Leike, A, "The Phenomenology of Extra Neutral gauge Bosons", Phys. Rept. 317 (1999), 143, [ArXiv:hep-ph/9805494].

[11] Benekos, N; Chevalier, L; Goldfarb, S; Harrington, R; Laporte, J F; Logashenko, I; Miller, J; Ouraou, A; Rebuzzi, D; Schott, M; Spagnolo, S; van Eldik, N; Verducci, M; Willocq, S, "Implementation of Chamber Misalignments and Deformations in the ATLAS Muon Spectrometer Simulation", Journal of Physics: Conference Series 119 (2008) 032010.